

# Journal of Geophysical Research: Oceans

## RESEARCH ARTICLE

10.1002/2018JC013764

### Special Section:

Sea State and Boundary Layer  
Physics of the Emerging Arctic  
Ocean

### Key Points:

- A Beaufort Sea autumn storm released a large amount of upper ocean heat, melting thin, new sea ice
- Heat release was larger than in prior studies under multiyear ice, with a greater role by atmospheric heat fluxes
- The forcing conditions in this event are related to the changing wave climate in the western Arctic Ocean

### Correspondence to:

M. Smith,  
mmsmith@uw.edu

### Citation:

Smith, M., Stammerjohn, S., Persson, O., Rainville, L., Liu, G., Perrie, W., et al. (2018). Episodic reversal of autumn ice advance caused by release of ocean heat in the Beaufort Sea. *Journal of Geophysical Research: Oceans*, 123, 3164–3185. <https://doi.org/10.1002/2018JC013764>

Received 29 DEC 2017

Accepted 5 MAR 2018

Accepted article online 12 MAR 2018

Published online 6 MAY 2018

## Episodic Reversal of Autumn Ice Advance Caused by Release of Ocean Heat in the Beaufort Sea

Madison Smith<sup>1</sup> , Sharon Stammerjohn<sup>2</sup> , Ola Persson<sup>3</sup> , Luc Rainville<sup>1</sup>, Guoqiang Liu<sup>4</sup>, William Perrie<sup>4</sup> , Robin Robertson<sup>5</sup> , Jennifer Jackson<sup>6</sup> , and Jim Thomson<sup>1</sup> 

<sup>1</sup>Applied Physics Laboratory, University of Washington, Seattle, WA, USA, <sup>2</sup>Institute of Arctic & Alpine Research, University of Colorado, Boulder, CO, USA, <sup>3</sup>NOAA/ESRL Physical Sciences Division, Boulder, CO, USA, <sup>4</sup>Bedford Institute of Oceanography, Fisheries & Oceans Canada, Dartmouth, NS, Canada, <sup>5</sup>China-ASEAN College of Marine Sciences, Xiamen University, Sepang, Selangor, Malaysia, <sup>6</sup>Hakai Science, Hakai Institute, Calvert Island, BC, Canada

**Abstract** High-resolution measurements of the air-ice-ocean system during an October 2015 event in the Beaufort Sea demonstrate how stored ocean heat can be released to temporarily reverse seasonal ice advance. Strong on-ice winds over a vast fetch caused mixing and release of heat from the upper ocean. This heat was sufficient to melt large areas of thin, newly formed pancake ice; an average of 10 MJ/m<sup>2</sup> was lost from the upper ocean in the study area, resulting in ~3–5 cm pancake sea ice melt. Heat and salt budgets create a consistent picture of the evolving air-ice-ocean system during this event, in both a fixed and ice-following (Lagrangian) reference frame. The heat lost from the upper ocean is large compared with prior observations of ocean heat flux under thick, multiyear Arctic sea ice. In contrast to prior studies, where almost all heat lost goes into ice melt, a significant portion of the ocean heat released in this event goes directly to the atmosphere, while the remainder (~30–40%) goes into melting sea ice. The magnitude of ocean mixing during this event may have been enhanced by large surface waves, reaching nearly 5 m at the peak, which are becoming increasingly common in the autumn Arctic Ocean. The wave effects are explored by comparing the air-ice-ocean evolution observed at short and long fetches, and a common scaling for Langmuir turbulence. After the event, the ocean mixed layer was deeper and cooler, and autumn ice formation resumed.

**Plain Language Summary** As Arctic Ocean temperatures drop below freezing in the autumn, sea ice begins to form, sealing off the ocean below. The ice's southward advance throughout autumn is not linear, however, as storm events may act to pause its progression. We observed a 4 day storm event in the western Arctic Ocean in October 2015 with strong winds (up to 20 m/s) and large waves (over 4 m). As a result, heat from the upper ocean was mixed to the surface, melting approximately 5 cm thick ice over a vast area. This event temporarily reversed autumn ice advance and resulted in a thinner winter ice cover. This study is the first to document autumn melt of sea ice by ocean heat in the thin, new ice that increasingly dominates in the Arctic Ocean. The magnitude of the heat lost is likely related to the large surface waves during this event that result from lower sea ice cover. These results highlight the importance of air-sea interactions in current and future Arctic sea ice cover.

## 1. Introduction

Autumn in the Arctic Ocean is characterized by decreasing temperatures, decreasing solar radiation, and strong heat fluxes from the ocean surface to the atmosphere. Areas of open water freeze as the sea ice advances southward, with ice formation largely controlled by changing atmospheric conditions and reduced solar input.

In recent decades, the total area of seasonally open water has expanded, and thus a greater area of ice advance is required to return to the full winter ice cover (Jeffries et al., 2013). This spatial signal is accompanied by a temporal one: the ice advance has also been occurring later each autumn (Meier, 2017; Stroeve et al., 2016). This is especially true in the Beaufort Sea, the marginal sea north of Alaska and western Canada that contains the southernmost part of the deep Canada Basin. For the Beaufort Sea in particular, the transition from open water to seasonal ice has been occurring an average of 1–2 days later per year, with a net shift of ice advance from 1979 to 2010 almost 1 month later in the climatology (Stammerjohn et al., 2012). This delayed ice advance is responsible for longer open water periods (Galley et al., 2016).

Some consequences of summer sea ice decline over the Canada Basin include enhanced surface wave generation, greater air-sea exchanges, and increased solar heating of the upper ocean. Large expanses of open water in the summer Arctic Ocean in recent years allow winds to form large swells that propagate into the ice pack (Asplin et al., 2012, 2014). Observations of discrete large wave events (Asplin et al., 2012; Collins et al., 2015; Thomson & Rogers, 2014) are indicative of a general shift in the wave climate toward larger waves in the Beaufort Sea (Stopa, 2016; Thomson et al., 2016). The extent to which the increasing wave climate has enhanced mixing in the surface waters, via mechanisms such as Langmuir turbulence (D'Asaro et al., 2014), is not known. Larger surface waves increase turbulent fluxes and gas exchange at the surface (Loose et al., 2009). In open water, there are significantly larger energy exchanges between the upper ocean and the atmosphere (Maykut, 1978). In the marginal ice zone, the area of transition between open ocean and sea ice pack, the high-frequency portion of the wave spectrum is suppressed (Zippel & Thomson, 2016). Although there are clear signals of these mechanical changes in the expanding marginal ice and open water zones, the thermodynamic feedbacks are not well understood.

The longer period of open water has delayed autumn ice advance by increasing the amount of solar radiation stored in the upper ocean (Jackson et al., 2010). The surface mixed layer in the Canada Basin is typically shallow (0–10 m) at the beginning of autumn. This is a result of freshwater input (sea ice melt and river input) and the lack of strong forcing (i.e., storms) to cause mixing during summer (Peralta-Ferriz & Woodgate, 2015). During summer in the Canada Basin, sea ice melts to form a stratified layer called the summer halocline that is typically observed at 10–20 m (Jackson et al., 2010). Stratification in the summer halocline traps solar radiation, forming a near-surface temperature maximum (NSTM) that typically resides at 20–35 m and is a common feature in the Beaufort Sea region of the Arctic Ocean (Maykut & McPhee, 1995). The NSTM typically has a salinity between 28 and 30 psu and is defined as being less than 31 psu (Jackson et al., 2010). It stores a substantial amount of heat, with an average of 0.24° above freezing in the eastern Canada Basin (as observed in October 2005; Jackson et al., 2010). Although the NSTM has been observed as a year-round feature, it normally deepens, cools, and disappears throughout the autumn and winter (Jackson et al., 2010; Steele et al., 2011). The saltier, cooler region below the NSTM is thought to be the remnant winter mixed layer from the prior year (rWML; Jackson et al., 2010). Below the rWML is Pacific Summer Water (PSW), which is a warm, relatively salty water mass, typically between 30 and 32 psu and over 0.5°C in the Canada Basin (McLaughlin et al., 2011).

Average temperatures of both the surface mixed layer and NSTM have been increasing as a result of longer open water season in recent decades, which provides increased opportunity for input of solar radiation to the upper ocean (Jackson et al., 2010; Perovich et al., 2007; Stroeve et al., 2014). In particular, the NSTM in the Canada Basin warmed by about 1.5° and freshened by about 4 psu from 1993 to 2009 (Jackson et al., 2011). Additionally, the summer halocline and NSTM have been shallower on average, with shoaling observed from 2002 to 2007 likely due to the increase of in situ sea ice melt (Jackson et al., 2010).

Various studies using ice mass balance buoys (IMBs) and ice-tethered profilers (ITPs) deployed on thick, multiyear ice floes in this region have shown entrainment of heat from the ocean mixed layer and NSTM to be a primary driver of sea ice melt through summer and autumn. Perovich et al. (2008) used IMB data to show that solar heating of the ocean was a primary driver for bottom melt of sea ice during the summer of 2007. Jackson et al. (2012) used ITPs deployed on 3 m thick ice floes north in the Canada Basin to show that solar heat stored in the NSTM during the following autumn and winter was periodically entrained into the mixed layer, corresponding to brief periods of bottom melt of thick sea ice. Similarly, Timmermans (2015) observed melt at the bottom of 3–4 m thick ice floes as a result of erosion of the NSTM. The correlation of ice thinning with loss of heat from the NSTM suggests that oceanic heat fluxes are causing sea ice melt and decreased winter ice growth. The ice melt that would be inferred from the total loss of ocean heat is only 20–60% more than the observed basal sea ice melt (Timmermans, 2015), indicating that the majority of upper ocean heat flux goes into the ice, rather than the atmosphere.

The seasonal entrainment of heat from the NSTM into the surface mixed layer in the Canada Basin is generally presumed to be a result of shear-driven mixing from wind and ice motion (Jackson et al., 2012). Strong wind or rapidly drifting ice causes relative motion between the surface mixed layer and NSTM, which results in mixing at the summer halocline. Although shear-driven mixing generally dominates, convective mixing due to salt plumes can occur under low ice-ocean relative velocities (Barthélemy et al., 2015). Convective mixing and overturning of the halocline as a result of brine rejection with sea ice growth has been observed by studies in the eastern Arctic Ocean, near Svalbard and Greenland (Ivanov et al., 2016; Roach et al., 1993), where the surface mixed layer in the eastern Arctic Ocean is on the order of 100 m deep with weak stratification (approximately 1 psu).

However, the characteristic temperature and salinity profiles in the Canada Basin have comparatively shallow, strongly stratified surface waters that further reduce the likelihood of convective mixing (McLaughlin et al., 2011). Even with rapid ice formation throughout autumn in the Beaufort Sea, mixing at the summer halocline and entrainment of heat from the NSTM is likely to result from high-wind events rather than brine rejection (Yang et al., 2004). In fact, it has been suggested that autumn storms, of increasing cyclonic intensity (Simmonds & Keay, 2009), are playing a significant role in the delay of ice edge advance via the release of upper ocean heat.

Although several previous studies have observed ocean mixing events causing sea ice melt under thick, multi-year ice floes, there are few prior observations of ocean-ice coupling under the thin ice that forms during autumn ice advance. As Arctic multiyear ice continues to decline, processes associated with new and first-year ice are becoming more important to the overall Arctic system. This study will use observations of a high-wind event over 5 days in the Beaufort Sea area of the Canada Basin to show how ocean heat can melt the thin, newly formed sea ice. First, we will describe the high-resolution measurements made from both ship transects and drifting buoys. Then, we will examine key terms in heat and salt budgets controlling sea ice melt and the temporary reversal of the autumn ice advance. In the discussion, we will explore how the net impact of this autumn event compares to ocean heat loss events previously observed beneath Arctic sea ice. Specifically, we will speculate how the thinner ice and the presence of large surface waves may enhance mixing and ocean heat flux, relative to prior results under thick multiyear ice floes in the absence of surface waves.

## 2. Observational Methods

A high-wind event was observed 10–14 October 2015 over the northern Beaufort Sea, in the deep Canada Basin, north of Alaska (Figure 1). Measurements were made from the *R/V Sikuliaq* as part of the Sea State

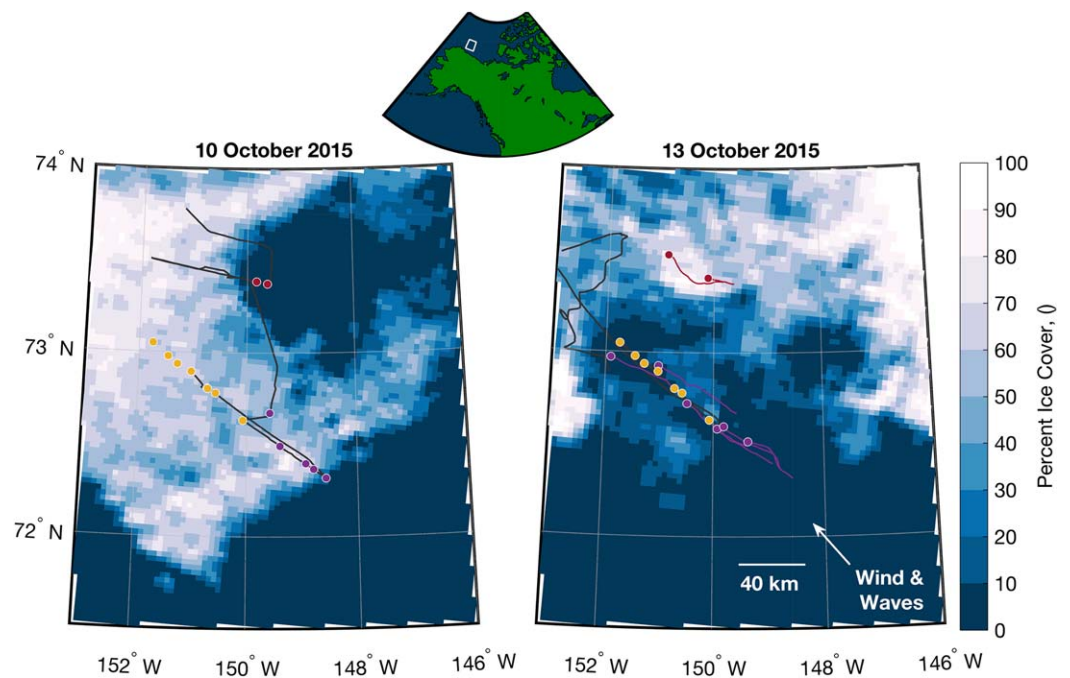


**Figure 1.** Ice concentration and measurement locations in the study area on (left) 10 October 2015 and (right) 13 October 2015. Sea ice concentrations are from 3.125 km daily AMSR2 satellite measurements (Spreen et al., 2008). Map inset at top shows location of study area. Initial measurement locations are shown on the left with the ship track (black line) from 10 to 11 October. Final measurement locations are shown on the right with the ship track from 12 to 14 October. The seven Eulerian locations, shown by gold dots, are (by definition) the same prior to and after the event. The main array of SWIFT buoys used for this analysis are shown by the six purple dots at the (left) initial and (right) final locations, with the intervening drift tracks shown by thin purple lines in the right figure. (Note a sixth SWIFT buoy location in the left figure is hidden behind a gold dot, third from right.) The two northern SWIFT buoys (indicated by red dots) will be revisited in the discussion. Buoy drift tracks are generally to the northwest during the event, in agreement with the wave direction and slightly to the right of the wind direction, with an average drift distance of 40 km to the northwest over the 3 days. The prevailing wind direction was 20°–30° to the left (west) of the drift direction.

**Table 1**  
Summary of Variables and Observational Methods From Ship-Based and Drifting Buoy (SWIFT) Platforms

Type	Variables	Method
<i>Ship-based (Eulerian)</i>		
Surface	Wind speed and direction	Metek 3-D
	Significant wave height	Reigl Lidar
Upper ocean	Temperature and salinity	OceanSciences uCTD
Sea ice	Sea ice concentration, thickness, and type	ASSIST visual protocol (Worby, 1999)
<i>Drifting SWIFTs (Lagrangian)</i>		
Surface	Wind speed and direction	Airmar PB200 sonic anemometer
	Wave spectra, height, period, and direction	Microstrain 3DM-GX3-35
Upper ocean	Temperature and salinity (0.5 m)	Aanderra CT
<i>Calculated</i>		
Surface	Net atmospheric heat flux ( $F_{atm}$ )	See Thomson et al. (2018) and references therein
Upper ocean	Heat content (HC)	Integrated uCTD profiles (equation (1))
	Salt content (SC)	Integrated uCTD profiles (equation (2))

Departmental Research Initiative (DRI) field campaign in the Beaufort-Chukchi Seas, from 1 October to 10 November 2015. Data acquisition during the entire cruise is described in the cruise report (Thomson, 2015) and in an overview paper (Thomson et al., 2018).

At the start of the event, on 10 October 2015, the ship arrived at the ice edge after transiting through over 100 km of newly formed pancake ice that characterized the initial ice cover. The extent of this pancake ice was remarkable, given the general rarity of pancake and granular ice formation previously observed in the Arctic (Eicken et al., 1995), and was evidence that surface wave forcing had occurred prior to our arrival. During the 4 day storm, a ship-based survey was conducted along a  $\sim 100$  km transect normal to the ice edge and parallel to the surface drift direction, within and just outside the changing ice cover. Measurements from the ship characterized the evolution of the atmosphere, ice, and upper ocean heat and salt during the event. Additionally, surface-following buoys (SWIFTs) were deployed to measure surface winds, waves, currents, temperature, and salinity; these generally drifted to the northwest. Figure 1 shows the initial (10 October) and final (13 October) ice concentrations, overlaid with the buoy positions, the axis of the drift, and several repeat stations from the ship's track. We first describe the measurements made from the ship, and then describe the measurements made by SWIFT buoys. Measurement platforms and associated variables are summarized in Table 1. These measurements allow us to assess changes in ocean heat content, particularly in relation to changes in ice cover. This is accomplished by combining ship-based and buoy observations, as the buoys drifted with the ice in a surface-Lagrangian reference frame (Lund et al., 2018), while the ship repeated stations in an Eulerian reference frame. Comparing the two reference frames allows for estimation of horizontal advection effects, and assessment of the space-time variability over the domain.

## 2.1. Ship-Based Measurements

### 2.1.1. Atmosphere Observations

Atmospheric forcing during the event is characterized using bulk meteorological observations and turbulent flux measurements by a suite of instruments installed on the ship's mast. The measurements will be only briefly summarized here. Full description of the field campaign and ship-based instrumentation can be found in Thomson et al. (2018) and references therein.

Wind speed ( $U_{10}$ ) and direction were measured from heated Metek 3-D ultrasonic anemometers sampling at 10 Hz installed at two heights on the ship's bow. Net atmospheric heat flux ( $F_{atm}$ ) is a combination of radiative, sensible, and latent heat fluxes; a complete time series is obtained from a combination of shipboard measurements and derived calculations (Persson, 2012). Evaporation at the surface is calculated using shipboard measurements of latent heat flux as  $E = \frac{LHF}{L_f \rho}$ , where  $L_f$  is latent heat of fusion of seawater and  $\rho$  is the density. Latent heat flux ( $LHF$ ) is measured using a Licor 7500



at 10 Hz. Scanning and fixed-point laser rangefinders (Riegl) were installed at the top of the tower for continuous underway measurements of significant wave height (Collins et al., 2017).

### 2.1.2. Upper Ocean Observations

Eulerian changes of the upper ocean are examined using temperature ( $T$ ) and salinity ( $S$ ) profiles from an OceanSciences underway CTD (uCTD). The uCTD was deployed off the stern of the ship while moving at speeds of 0.5–3 m/s approximately once hourly, as ice conditions and ship speed allowed. Vertical profiles were generally acquired over 5–150 m depth; the top 5 m of data are excluded to eliminate contamination from the ship's wake. Data have been processed to correct for the different lagged responses of temperature and conductivity sensors with a variable fall rate, including recomputing salinity from the lag-corrected temperature and conductivity values (e.g., Ullman & Hebert, 2014).

The mixed layer depth (MLD) is identified for uCTD profiles. There have been a variety of different methods used in the literature for determining the MLD. Here we identify the MLD as the shallowest depth at which potential density is more than  $0.1 \text{ kg m}^{-3}$  greater than the near-surface mean potential density. This method was selected by Peralta-Ferriz and Woodgate (2015), who reviewed Arctic Ocean mixed layer properties and determined that this method agreed well with visual assessments of MLD. Near-surface mean potential density is calculated as the average over the upper 10 m to account for noisy near-surface density profiles, and is calculated here from 5 to 10 m to avoid bias from the ship's wake. Density is used instead of temperature in the Arctic Ocean, as the salinity has a strong impact on density (Steele et al., 2011). The temperature maximum below the MLD is identified as the near-surface temperature maximum (NSTM) following the definition in Jackson et al. (2010). The temperature minimum below the NSTM is identified as remnant winter mixed layer (rWML; Jackson et al., 2011). Below this is another temperature maximum in the Pacific Summer Water (PSW) layer.

### 2.1.3. Sea Ice Observations

Sea ice cover characteristics were recorded hourly from visual observations made from the bridge, including the average sea ice concentration, thickness, and type within 0.5 nautical mile of the ship. At night, observations were aided by use of the ship's flood lights. Observations were made following the ASSIST protocol, which provides a standardized way to make and record sea ice observations in the Arctic Ocean, and is based on the ASPECT protocol developed for the Southern Ocean (Worby, 1999). Such visual estimates have been shown to be reasonably accurate, with error of approximately 30% for ice thickness less than 30 cm and approximately 10% for ice concentration (Worby et al., 2008). Ice thickness estimates are validated with physical samples collected hourly using a dip net over the side of the ship and measured on deck (Wadhams et al., 2018). Ice concentration estimates are validated with images collected from SWIFT buoys every 4 s (effective during daylight hours only) whenever spatially and temporally collocated (see section 2.4).

An effective ice thickness,  $ice_{obs}$ , is calculated as  $ice_{obs} = IC_{obs} \times z_{ice}$ , where  $z_{ice}$  is the visually estimated ice thickness and  $IC_{obs}$  is the visually estimated ice concentration. Change in effective ice thickness at a location,  $\Delta ice_{obs}$ , is calculated as the difference in initial and final observed concentrations multiplied by ice thickness.

### 2.2. Drifting Buoy Observations

Lagrangian observations of surface winds, waves, temperature, and salinity were made using version 3 (v3) Surface Wave Instrument Floats with Tracking (SWIFTs). SWIFTs are freely drifting buoys originally designed to measure surface turbulence (Thomson, 2012). Observations occur in 8 min bursts of raw data collection 5 times an hour and are postprocessed into half-hour intervals for bulk statistical quantities.

SWIFTs have a draft of 1.2 m and thus drift with the surface currents. Lund et al. (2018) show that SWIFT drift velocities are within 1–2% of ice drift velocities, resulting in less than a half kilometer difference in distance traveled over the approximately 4 day deployment. As the spatial scales considered here are on the scale of tens of kilometers, SWIFT measurements are considered to be in an ice-following reference frame.

The main buoy array consisted of six buoys that drifted along a transect approximately aligned perpendicular to the waves and  $\sim 20^\circ$ – $30^\circ$  to the right of the wind direction from  $72.3^\circ\text{N}$ ,  $148.5^\circ\text{W}$  to  $73.0^\circ\text{N}$ ,  $152.6^\circ\text{W}$ . The deployments spanned from early on 11 October to late on 13 October, with initial (deployed) and final (retrieved) locations shown by purple dots in Figure 1. All buoys drifted to the northwest during the event.

**Table 2**  
Comparison of Forcings for Main Array and Northern SWIFT Buoys

	Main array		North buoys	
$U_{10}$ (m/s)	10–18		10–15	
$H_s$ (m)	2–5		1–3	
	Initial	Final	Initial	Final
$Ice_{obs}$ (cm)	4	1	1	4
Ocean HC (MJ/m <sup>2</sup> )	20	9	35	?

Two buoys were deployed on 10 October at approximately 73.4°N, 150.0°W, to the north of the main observation area; these are colored red in Figure 1. These drifted in the same direction as the other six SWIFT buoys and parallel to the Eulerian ship track points (with drift tracks shown as thin colored lines in right figure) but are located ~65 km north of the main array. Note that the ice concentration surrounding these two northern buoys actually increased from 10 October to 13 October, in contrast to the other six buoys (Table 2). These buoys will not be used in the analysis of this event but will be revisited in section 4. The main array buoys were deployed in order to span the initial ice conditions from open water

to thick pancake ice, while northern SWIFT buoys were within an open embayment that subsequently became ice covered.

Measurements of local wind speed and direction are made from an Airmar PB200 ultrasonic anemometer on the mast of each SWIFT, 1 meter above the ocean surface. Ice buildup on the sensors occasionally results in spurious wind measurements (identifiable by high variance), and these values are removed in postprocessing. Surface wind speeds ( $U_1$ ) are corrected to 10 m above surface by  $U_{10} = 1.19U_1$ , as the bulk estimates of  $u_*$  and  $R_{ib}$  suggest that a multiplicative factor of 1.14–1.23 is appropriate for the atmospheric conditions observed (Sellers, 1974). Each buoy also acquires images of the ocean surface from the mast every 4 s using a uCAM serial camera. Images are useful for observing local ice conditions (e.g., Rogers et al., 2016), although temporal coverage is severely limited by daylight and formation of ice on camera lenses. Water temperature and salinity are measured 0.5 m below the surface using an AADI Aanderaa Conductivity Sensor (model 4319).

Measurements of horizontal wave orbital displacements from a surface-following buoy can be used to infer the wave spectra based on linear wave theory, where it is assumed that wave orbitals are circular (Herbers et al., 2012). Horizontal displacements are made by the SWIFT using a Microstrain 3DM-GX3–35 combination GPS receiver and Inertial Motion Unit (IMU). Wave orbital velocity components are measured with a horizontal precision of 0.05 m/s, which is sufficient to capture orbitals of most ocean waves (as most orbital velocities are on the order of meters per second), and at a frequency of 4 Hz. Spectral estimates of wave energy are calculated by applying a Fast Fourier Transform (FFT) with four windows with 75% overlap, then ensemble averaging (e.g., Forristall, 1981). Further details on wave measurements from this platform can be found in Thomson (2012).

Bulk wave parameters are used to give a general characterization of the wave conditions and are calculated from wave energy spectra as follows. Significant wave height describes the surface elevation associated with the wave field and is defined as  $H_s = 4\sqrt{m_0}$ —four times the square root of the zeroth moment of the wave spectra (i.e., the total variance). Wave period ( $T_p$ ) is defined as inverse of the energy-weighted frequency ( $f_e$ ),  $f_e = \frac{\sum E_f}{m_0}$ . Peak wave direction describes the direction of wave propagation and is determined as the maximum in the wave directional distribution, calculated from directional moments using the maximum entropy method (Lygre & Krogstad, 1986).

### 2.3. Heat and Salt Budgets

The heat and salt content of the upper ocean is expected to change over the course of the event as a result of the formation or loss of sea ice, and exchange with the stratified layers below and the atmosphere above. Observed one-dimensional changes in heat and salt content of an ocean layer are defined as  $\Delta HC$  and  $\Delta SC$  and can be estimated by integration of upper ocean profiles as

$$\Delta HC = \Delta \int_h^0 \rho c_p (T(z) - T_{fr}) dz = c_p (\rho_{final} \int_h^0 (T_{final}(z) - T_{fr}) - \rho_0 \int_h^0 (T_0(z) - T_{fr})), \quad (1)$$

$$\Delta SC = \Delta \int_h^0 \rho (S - \bar{S}_{ML}) dz = \rho_{final} \int_h^0 (S_{final}(z) - \bar{S}_{ML}) - \rho_0 \int_h^0 (S_0(z) - \bar{S}_{ML}), \quad (2)$$

where  $c_p$  is the volumetric heat capacity of water,  $\rho$  is the average potential density,  $T(z)$  and  $S(z)$  are measured uCTD temperature and salinity profiles, and subscript 0 indicates the initial profile. Observed changes are calculated over the upper ocean to the depth  $h$  of the 1,022 kg/m<sup>3</sup> isopycnal, which is generally below

the final MLD. The choice of this integration depth is explored in Appendix A. Change in heat content is calculated using the temperature relative to the freezing temperature,  $T_{fr}$ , the latter determined using observed salinity. Similarly, change in salt content is calculated using the salinity relative to the average salinity in the initial mixed layer,  $\bar{S}_{ML}$ , where MLD is defined as the shallowest depth at which potential density is  $0.1 \text{ kg/m}^3$  greater than the near-surface potential density. This is necessary to account for vertical motion resulting in thickening of the mixed layer (as with inertial pumping).

One-dimensional heat and salt budgets are used to understand fluxes in the upper ocean during the event and, in particular, the relationship with changes in amount of sea ice cover. Full heat and salt budgets consider all mechanisms for changing heat or salt in a volume of water. The surface mixed layer heat budget proposed in Cronin et al. (2013) for use in the subtropical Pacific Ocean is adapted for use here, similar to that used in the eastern Arctic in Polyakov et al. (2013):

$$\Delta HC = \Delta t \underbrace{(F_{atm} - F_{ice})}_{1: \text{heat fluxes}} - \underbrace{\rho C_p h \bar{u} \cdot \nabla_H \bar{T}}_{2: \text{horizontal advection}} - \underbrace{\rho C_p \overline{w' T'}}_{3: \text{turbulent flux}}|_{z=h}. \quad (3)$$

Term 1 on the RHS includes the atmospheric heat fluxes into/out of the ocean surface ( $F_{atm}$ ), and the heat fluxes corresponding to the formation or loss of sea ice ( $F_{ice}$ ). Term 2 represents horizontal (lateral) advection due to average horizontal velocity ( $\bar{u}$ ) over horizontal gradients in the temperature profiles ( $\nabla_H \bar{T}$ ). Term 3 is the turbulent flux, alternatively referred to as diffusive mixing, which transports heat vertically. Estimation of these terms will be discussed further in section 3. This heat budget differs from that used by Cronin et al. (2013) and Polyakov et al. (2013) in the inclusion of the heat flux to/from ice (i.e., Timmermans, 2015), and the exclusion of a vertical advection term. When constraining the heat budget to an isopycnal below the mixed layer, the vertical advection term (which would otherwise be large) becomes unnecessary.

The salt budget proposed in Cronin et al. (2015) is adapted for use here as

$$\Delta SC = \Delta t \underbrace{\rho(E - P)S_0}_{1: \text{evap. \& precip}} - \underbrace{\rho_{ice} S_{ice} \Delta ice_{obs}}_{2: \text{ice source/sink}} - \underbrace{\Delta t \rho h \bar{u} \cdot \nabla \bar{S}}_{3: \text{horizontal advection}} - \underbrace{\Delta t \rho \overline{w' S'}}_{4: \text{turbulent flux}}|_{z=h}, \quad (4)$$

where term 1 represents evaporation and precipitation at the surface ( $E$  and  $P$ ), with  $S_0$  being the salinity at the surface. Term 2 is the change in salinity due to ice growth or melt and is based on the salinity of the ice ( $S_{ice}$ ) and the change in effective thickness of the ice ( $ice_{obs}$ ). Terms 3 and 4 represent the processes of horizontal advection and turbulent fluxes, respectively (as described for the heat budget). As with the heat budget, the primary difference between this salt budget and that used in Cronin et al. (2015) is the inclusion of salinity changes associated with growth or melt of sea ice (term 2) and the exclusion of vertical advection justified by constraining the budget to an isopycnal.

Budgets are applied over the upper ocean from the surface down to the  $1,022 \text{ kg/m}^3$  isopycnal. Use of alternative depths  $h$ , as discussed in Appendix A, changes the balance of terms in the heat and salt budgets but does not significantly change the conclusions.

## 2.4. Reference Frames

Heat and salt budgets are calculated for both Eulerian (fixed stations revisited by the ship) and Lagrangian (SWIFT buoys drifting with the ice) reference frames. Variables required to calculate these budgets for both reference frames are net atmospheric heat fluxes, evaporation and precipitation, change in effective ice thickness, and upper ocean heat and salt content. For the Eulerian reference frame, all measurements were measured aboard the ship. For the Lagrangian reference frame, variables not directly measured by the SWIFT buoy are estimated by collocating ship-based measurements with locations of each drifting buoy time series.

The shipboard measurements are collocated with SWIFT buoy time series' whenever ship and buoys were within 20 km and 3 h. These cutoffs were chosen to be as restrictive as possible while still allowing a corresponding initial and final uCTD profile to be identified for each SWIFT buoy. This allows the shipboard measurements to be interpreted in an ice-following (Lagrangian) reference frame, and in particular to obtain initial and final uCTD profiles giving change in upper ocean heat content ( $\Delta HC$ ) and salt content ( $\Delta SC$ ) along a SWIFT drift track. While it should be noted that the 20 km threshold may represent a large spatial gradient of the observed ice and ocean conditions, the distance between initial and final uCTD profiles collocated

with SWIFTs is no more than 10 km different from the distance between initial and final SWIFT locations over the same period. In this way, SWIFTs are providing a translation distance in order to be considered Lagrangian and in an ice-following reference frame. Additionally, the gradients within a 20 km spacing were observed to be less than the gradients observed between initial and final locations, which were generally between 40 and 80 km apart.

### 3. Results

#### 3.1. Atmospheric Forcing

The sea level pressure analysis from the European Center for Medium Range Weather Forecasting showed a strong pressure gradient between a high pressure center over the ice to the northeast of the study area and a weak, disorganized, transient area of low pressure over northern and central Alaska. There was no distinct frontal passage, nor well-developed cyclone with this strong wind event; the minimum sea level pressure measured by the ship was 999 mb near 12 October 14 UTC.

Strong surface winds were observed from 11 to 14 October over the approximately 100 km  $\times$  100 km study area. Observed winds 16.5 m above the ocean surface were generally over 10 m/s, reaching a maximum of nearly 18 m/s, and were associated with a complex, bimodal low-level atmospheric jet structure, with one maximum ( $\sim$ 19 m/s) centered near 300 m and the other ( $\sim$ 18 m/s) near the top of the atmospheric mixed layer at 900 m height (e.g., see Guest et al., 2018, Figure 2). Winds decreased above this height, such that strong winds were only observed in the lowest 2 km of the troposphere throughout the entire event.

#### 3.2. Upper Ocean Evolution

The local evolution of the event, as observed in the Eulerian frame, is shown in Figure 2. Winds started increasing on 10 October and reached a maximum intensity along the ship track of 17 m/s early on 12 October (Figure 2a; black line). A long fetch of open ocean ( $\sim$ 400 km) extended to the E and SE of the measurement area, to the Alaskan coastline (see inset in Figure 1), allowing the strong winds to produce increasing wave heights starting near 11 October 00 UTC and reaching a maximum wave height estimated by Lidar of nearly 5 m from midday 11 October through 12 October (Figure 2a; gold line). The wave evolution generally followed the wind speed, with maximum wave heights of 4–5 m and wave periods of 8.6 s (not shown) coinciding with maximum winds. Atmospheric heat fluxes were negative throughout the event, where negative fluxes indicate loss of heat from the ocean surface, and averaged about  $-90$  W/m<sup>2</sup> after midday 11 October (Figure 2b). The early portion of the storm had large heat losses stronger than  $-230$  W/m<sup>2</sup> due to a large nighttime sensible heat flux, while the daytime heat losses during the event ( $\sim$ hours 18 UTC–02 UTC) were smaller ( $-50$  to  $-5$  W/m<sup>2</sup>).

Despite negative surface heat fluxes to the atmosphere, observed effective ice thickness decreased from 5–10 to 0–7 cm at the seven Eulerian stations that were revisited by the ship (Figure 2c; black points). Simultaneously, the upper ocean heat content (HC) calculated following equation (1) decreased from 17–33 to 4–18 MJ/m<sup>2</sup> (Figure 2c; gold points). The time-depth temperature field along the ship track (Figure 2d) shows this to be a result of cooling of the mixed layer, where the MLD and 1,022 kg/m<sup>3</sup> isopycnal are identified by thick and thin black lines, respectively. Convergence of the MLD and 1,022 kg/m<sup>3</sup> over time indicate entrainment of the top of the NSTM. Even after entrainment of heat from the NSTM to the mixed layer, heat was lost at the surface. The overall implication is that the ocean lost heat to both the ice (which melted as a result) and to the atmosphere.

SWIFT buoys drifting with the sea ice during the event (Lund et al., 2018) provide observations of the upper ocean in the Lagrangian reference frame, as shown in Figure 3. Wind speed measured by SWIFT buoys peaked at 17–20 m/s on the 12th (Figure 3a; black lines) and are comparable to those measured from the ship (Figure 2a) but with more spatial variability. The wind direction was initially from 95°E, and veered slightly southerly to 120° by early October 13 (not shown). The buoys drifted 20°–30° to the right of the wind; hence, the buoy drift tracks and ship line were oriented approximately ESE–WNW (Figure 1). The variation in wind speed and wave heights in the buoy reference frame show that the sea state evolved through both space and time. Spatial gradients in the waves were caused by interactions with the pancake ice, as described by Rogers et al. (2016), with a net result of smaller wave heights (Figure 3a; purple lines) and longer wave periods (not shown) farther into the ice.



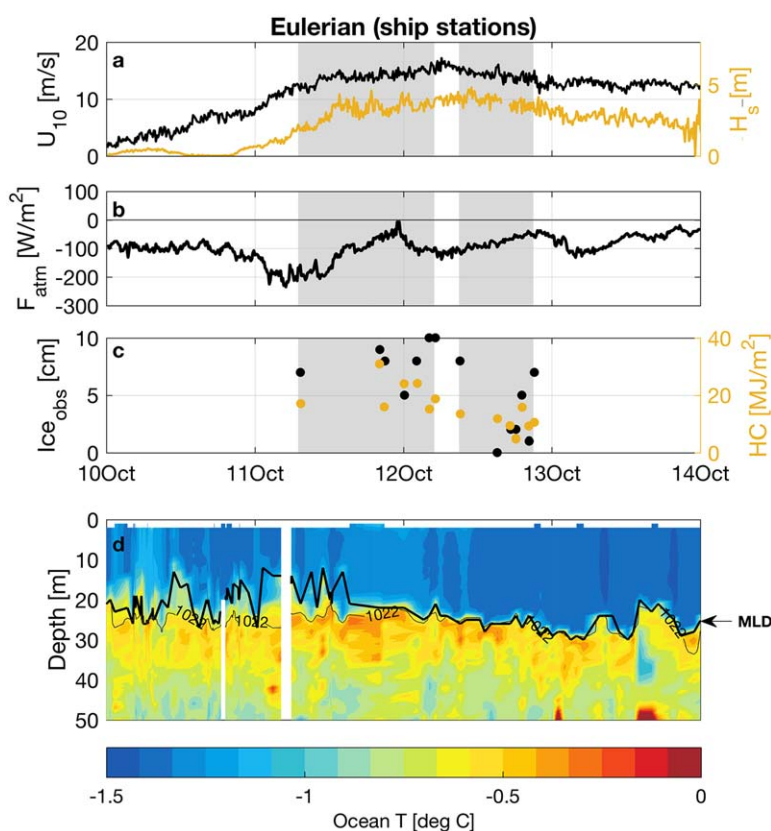


**Figure 2.** Time series for 10 to 14 October 2015 (UTC) of measurements in Eulerian reference frame (ship-based) of (a) 10 m wind speed (black) and significant wave height (gold), (b) net atmospheric heat flux, (c) effective ice thickness calculated from visual estimates of ice concentration and ice thickness (black) and heat content over the upper ocean (gold), and (d) upper ocean time-depth temperature field. MLD and 1,022  $kg/m^3$  isopycnal are identified on the temperature field as thick and thin black lines, respectively. Effective ice thickness and heat content are shown at Eulerian stations only, while all other variables are shown over the entire ship track. Grey shaded areas identify initial and final measurements used in Eulerian heat and salt budgets.

The sea ice and upper ocean are expected to move approximately with drifting buoys in the Lagrangian reference frame. As in the Eulerian reference frame, negative net atmospheric heat fluxes indicate that heat is being lost from the ocean surface to the atmosphere (Figure 3b). Yet sea ice effective thickness decreases from 0.8–4.2 to 0–1.5 cm (black points in Figure 3c). The observed decrease in ice is associated with a substantial decline in upper ocean heat content (purple points in Figure 3c). By the time the buoys are recovered, the mixed layer is nearly uniformly at the freezing temperature (Figure 3d). Again, the implication is that the ocean lost heat to both the ice (which melted as a result) and to the atmosphere.

In both Lagrangian and Eulerian reference frames, pairs of initial and final temperature at all measurement locations show a loss of heat from the upper ocean (Figure 4). Heat is removed from the mixed layer, such that final mixed layers are nearly uniformly at the freezing point. Some erosion of heat from the NSTM is observed. Pairs of initial and final salinity profiles in Lagrangian and Eulerian reference frames show that the mixed layer undergoes slight freshening, especially in the Lagrangian reference frame, due to freshwater input from sea ice melt. Offset of the 1,022  $kg/m^3$  isopycnal between initial and final profiles (grey and black points) is believed to primarily result from downward vertical advection of the upper ocean. Vertical advection likely results from inertial pumping, which is defined as upwelling or downwelling at or near the inertial period as a result of divergence in the surface velocity field. Divergence in surface velocities may result from a spatial gradient in sea ice and associated wind stress (Khandekar, 1980). The observed horizontal convergence of Lagrangian drifters is consistent with the amount of inertial pumping required to create the vertical offsets observed.

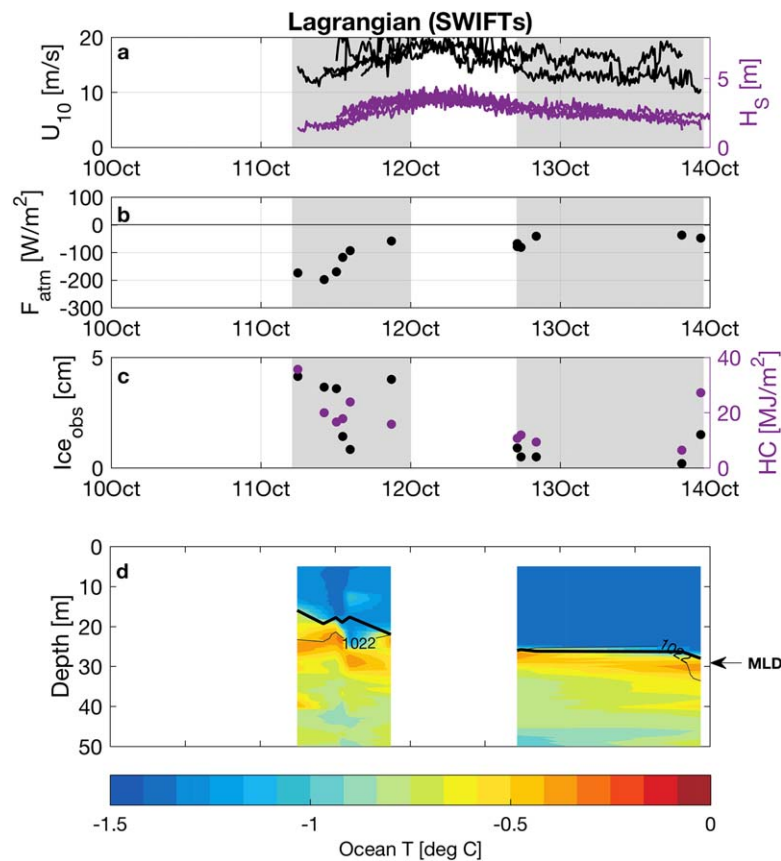


**Figure 3.** Time series from 10 to 14 October 2015 (UTC) in Lagrangian reference frame (main array of SWIFT buoys) of (a) 10 m wind speed (black) and significant wave height (purple), (b) net atmospheric heat flux, (c) effective ice thickness (black) and heat content (purple) over the upper ocean, and (d) upper ocean time-depth temperature field. MLD and 1,022  $kg/m^3$  isopycnal are identified as thick and thin black lines, respectively. Grey shaded areas identify initial and final measurements used in Lagrangian heat and salt budgets.

All initial and final upper ocean profiles shown in Figure 4 are also plotted as T-S diagrams with water masses identified in Figure 5. The T-S diagram corresponding to Lagrangian profiles also includes measurements of temperature and salinity 0.5 m below the surface from the SWIFTS. (These shallow depths are contaminated by the wake of the ship in the uCTD data set, and thus are only available from the SWIFTS.) T-S diagrams avoid isopycnal displacement problems by plotting temperature as a function of salinity, which sets the density in this area. Measurements in the surface mixed layer are clustered near the freezing point (dashed line), and the NSTM and PSW are identifiable as local temperature maxima. Comparing the initial (grey points) and final (black points) measurements show erosion of the NSTM and a more distinct transition between surface waters (in the mixed layer) and the NSTM below, especially in the Eulerian reference frame. NSTM, PSW, and water masses below PSW are spatially variable, evidenced by the spread of points.

### 3.3. Heat and Salt Budgets

The link between the upper ocean evolution and sea ice melt is evaluated using the heat and salt budgets defined in equations (3) and (4). Temperature and salinity profiles paired at fixed (Eulerian) and drifting (Lagrangian) locations (see Figure 4) are integrated to obtain changes in heat content ( $\Delta HC$ ) and salt content ( $\Delta SC$ ). The overall results are a substantial loss of heat and a negligible or minor salinification. Each of the terms on the right-hand side (RHS) of the budgets in equations (3) and (4) are calculated and considered in turn. The balance of the changes in upper ocean heat and salt content are summarized in Figure 6 (left and right, respectively), with error bars showing the standard deviation from each set of estimates.

Fluxes to the atmosphere (term 1 in the heat and salt budgets; turquoise bar in Figure 6) are estimated with ship-based instrumentation (Thomson et al., 2018, and references therein). The average heat flux out of the

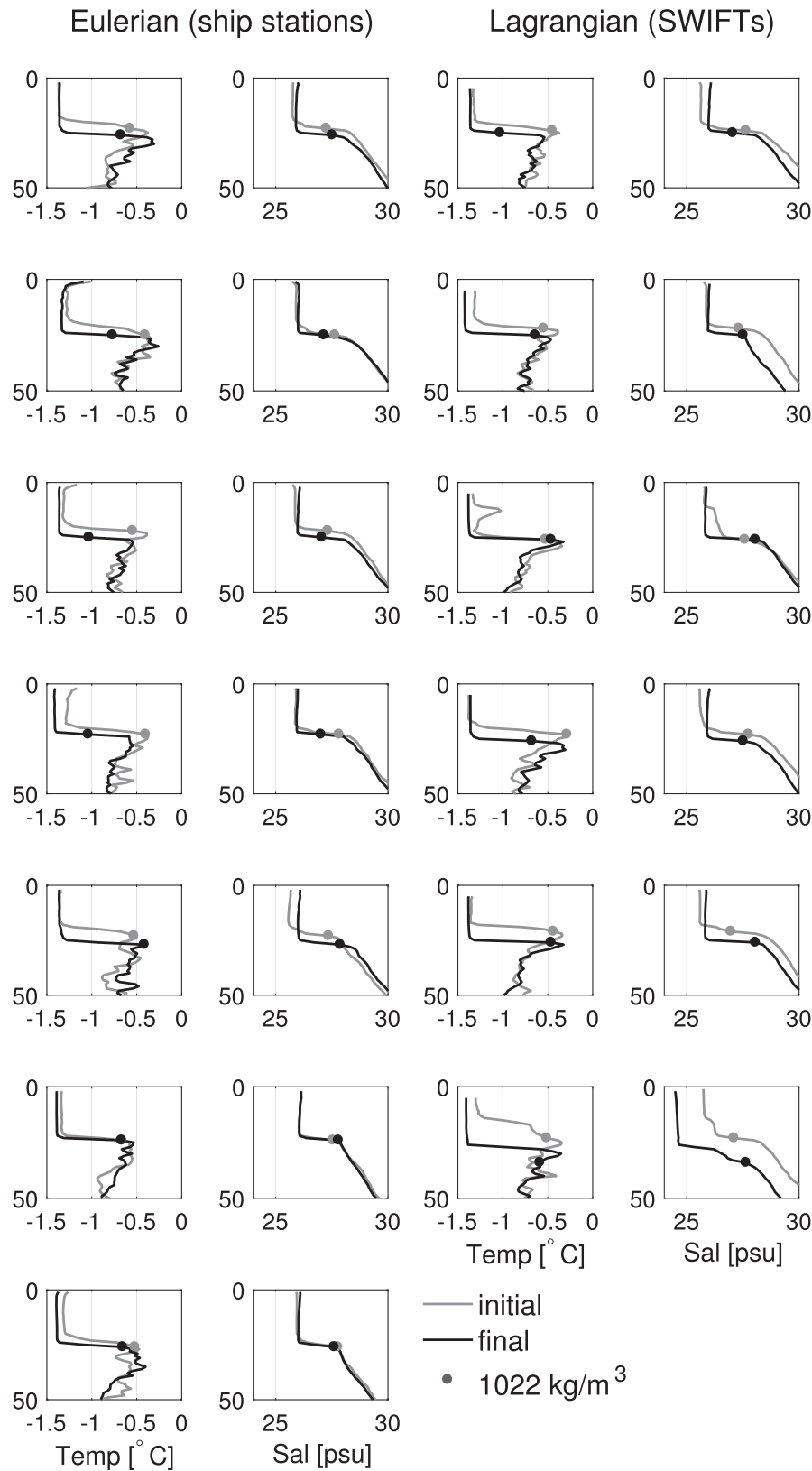


**Figure 4.** Temperature and salinity profiles at initial (grey) and final (black) times for all stations (seven total) and buoys (six total). Profiles are shown for Eulerian (ship-based) reference frame on the left, and for Lagrangian (SWIFT-following) reference frame on the right. Points mark a density of  $1,022 \text{ kg/m}^3$ , which is the bottom of the upper ocean layer to which budgets are applied.

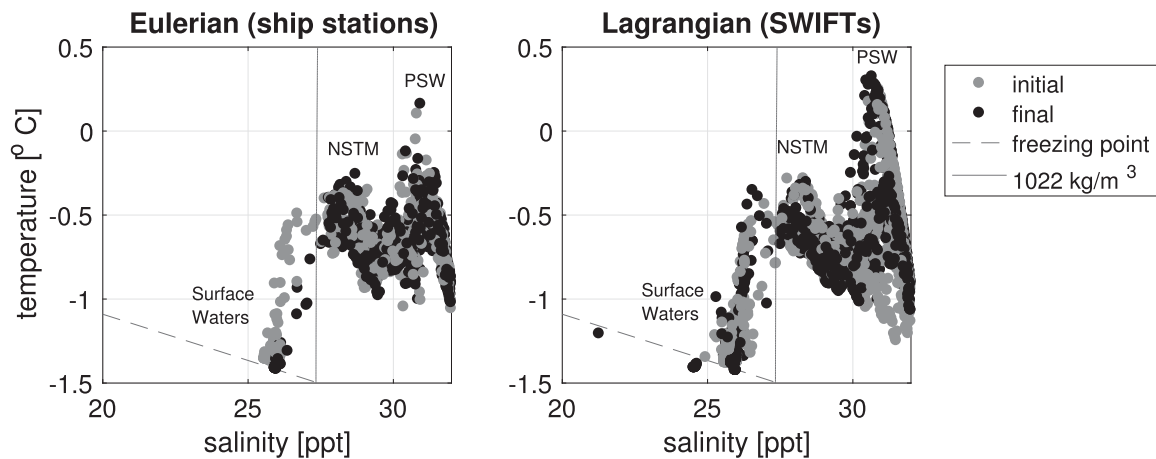


**Figure 5.** Temperature-salinity diagrams for initial (grey points) and final (black points) measurements, in both (left) Eulerian reference frame and (right) Lagrangian reference frame. The depth of measurements increases to the right, from 5 to approximately 80 m, as density is primarily a function of salinity. In the Lagrangian reference frame, SWIFT measurements of temperature and salinity at 0.5 m (below surface) are also included. The dashed line indicates the seawater freezing point at atmospheric surface pressure, and the thin vertical line represents a density of  $1,022 \text{ kg/m}^3$ . Surface waters (within the mixed layer), the near-surface temperature maximum (NSTM), and Pacific Summer Water (PSW) are also identified.

ocean surface is estimated for each profile as an average of collocated ship-based net atmospheric heat flux ( $F_{atm}$ ). Average values are larger in the Lagrangian reference frame than the Eulerian primarily due to the longer time period covered ( $\Delta t$ ). Precipitation was observed to be zero for all stations and SWIFTs locations during the event. Average observed evaporation from the surface of  $1.3\text{--}1.5 \times 10^{-4} \text{ m/s}$  leads to a minor salinity increase at all locations.

Loss of heat due to the loss of sea ice (term 1 in the heat budget and terms 2 in the salt budget; blue bar in Figure 6) is calculated with  $F_{ice} = \rho L_f \Delta ice_{obs}$  where  $\Delta ice_{obs}$  is the change in effective thickness from visual observations. Ice density is estimated to be  $938 \text{ kg/m}^3$  following Weeks and Ackley (1986) with an assumed brine volume of 36% and bubble fraction of 1%, and latent heat of fusion is estimated to be  $215 \text{ kJ/kg}$  following Ono (1966). Corresponding changes in observed ice thickness ( $\Delta ice_{obs}$ ) at the location of each

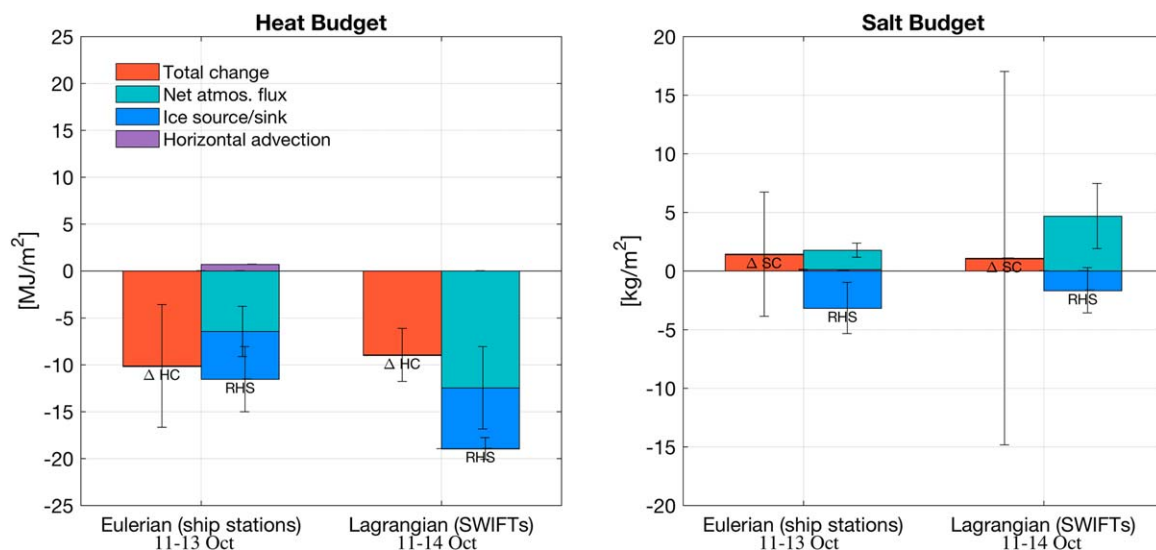


**Figure 6.** (left) Upper ocean heat budget and (right) salt budget for seven Eulerian ship stations, and six Lagrangian SWIFT buoys. For each pair of bars, observed changes in mixed layer heat ( $\Delta HC$ ) and salt content ( $\Delta SC$ ) calculated using collocated uCTD profiles are shown on the left, while estimates of RHS terms—net atmospheric fluxes, ice source/sink, and horizontal advection—are shown on the right (equations (3) and (4)). Negative values represent loss of heat and salt from upper ocean, respectively. Error bars are the standard deviation from each set of estimates. Details describing the terms and their calculations can be found in sections 2 and 3.

profile are calculated as the change in effective ice thickness; that is, the observed ice concentration multiplied by the average ice thickness observed. Similarly, salinity flux due to the loss of sea ice is calculated based on observed change in effective thickness as given in equation (4); a salinity of 6 ppt is used for sea ice ( $S_{ice}$ ), based on average measurements of ice collected with the dipnet during the event (Wadhams et al., 2018).

Horizontal advection describes the effect of spatial variability in upper ocean structure and sea ice (term 2 in the heat budget and term 3 in the salt budget; purple bars in Figure 6), and so may be represented by the difference of the observed changes in Eulerian and Lagrangian reference frames. As the upper ocean moves approximately with the Lagrangian buoys, this provides an estimate of the effect on the Eulerian (fixed) reference frame. Estimates of changes in heat and salt content due to horizontal advection of the upper ocean are calculated as the difference between Eulerian points closest to the final SWIFT locations (4–7) and Eulerian points closest to the initial SWIFT locations (1–3). This difference is scaled by the ratio of temporal coverage of the Eulerian and Lagrangian budgets. The horizontal advection term accounts for a small positive change in heat and salt content in Eulerian reference frame as a result of some spatial variability in initial mixed layer temperature and salinity. Although this estimate neglects much of the spatial and temporal variability of the event, the small value indicates that the role of horizontal advection on the depths being considered is negligible compared to the other terms.

Finally, the turbulent fluxes in the upper ocean (final terms in equations (3) and (4)) are estimated to be negligible. Following Cronin et al. (2015), turbulent heat and salt fluxes can be approximated using diffusivity constants  $\kappa_T$  and  $\kappa_S$  as

$$\begin{aligned}\rho C_p \overline{w'T'}|_{z=h} &= -\kappa_T \frac{\partial T}{\partial z}|_{z=h} \\ \rho C_p \overline{w'S'}|_{z=h} &= -\kappa_S \frac{\partial S}{\partial z}|_{z=h}\end{aligned}\quad (5)$$

Jackson et al. (2011) found diffusivity constant of  $\kappa_T \approx 3 \times 10^{-6}$  to realistically replicate temperature changes in the near-surface waters of the Canada Basin. Estimation of turbulent (diffusive) heat flux using these values gives heat content change on the order of 0.1 MJ/m<sup>2</sup> for this event, approximately 2 orders of magnitude smaller than the heat content change observed. We therefore assume that the turbulent flux term in the heat and salt budgets is negligible at all the measurement locations.

Overall, the results of the two reference frames are consistent: loss of heat from the upper ocean corresponds to the loss of sea ice at the surface. There was a significant loss of mixed layer heat and erosion of the NSTM over approximately 2 days that can be mostly accounted for by heat flux into the atmosphere and melting of surface sea ice. Of the total ocean heat lost, approximately 60–70% went into the atmosphere, and 30–40% went into melting sea ice (Figure 6). Thus, the observed changes in heat content are primarily driven by heat fluxes from the ocean to the ice and atmosphere (i.e.,  $\Delta HC \approx \Delta t(F_{atm} - F_{ice})$ ). Horizontal variability and turbulent fluxes have small and negligible effects during this event, respectively. The minor change in salt content in both reference frames can be accounted for by the balance of evaporation (increasing salt), and melting ice (freshening).

## 4. Discussion

### 4.1. Comparison to Prior Studies

Prior studies under thick, multiyear ice in the Canada Basin have also observed upper ocean heat loss that results in sea ice melt. Stored ocean heat is a result of solar input throughout the summer and early autumn that becomes trapped by stratification. Heat can become entrained into the surface mixed layer when mixing erodes the stratification in autumn and winter. Timmermans (2015) and Jackson et al. (2012) described entrainment of heat from the upper ocean during 2006–2008 and 2007–2008, respectively and found substantial fluxes of ocean heat to sea ice during high-wind events. The event described here has similar mechanisms to these previously described autumn entrainment events. However, previous studies used measurements from ITPs, which by definition must be deployed on thick ice floes, while the present study used ship-based measurements and ocean buoys to study changes in thin, pancake sea ice. As a result, there are key differences in the surface conditions, the magnitude of the heat fluxes observed, and the outcomes.



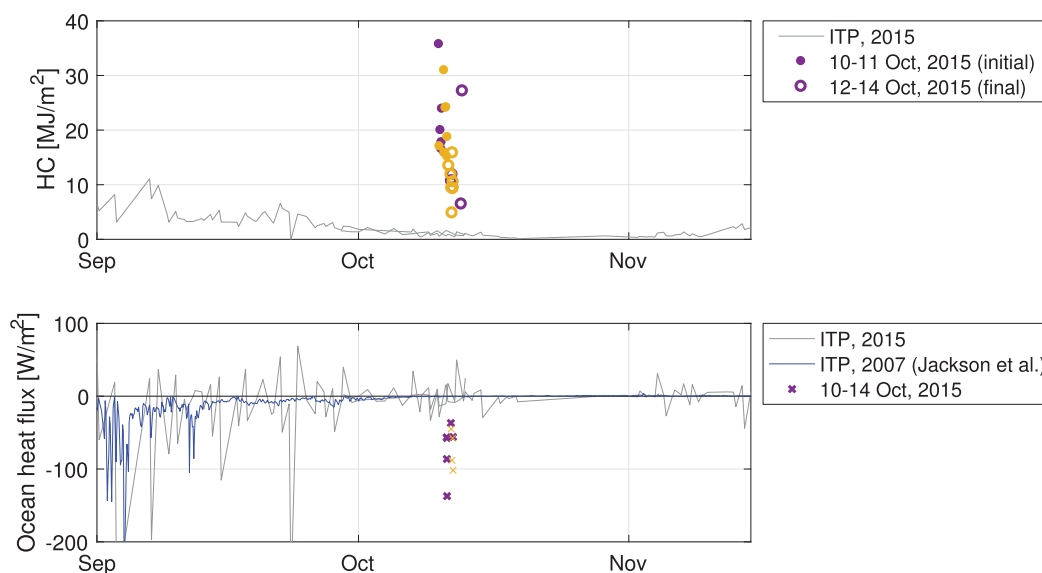


**Figure 7.** Comparison of ocean heat content (HC) and heat flux observed during autumn in the Canada Basin from four ice-tethered profilers (ITPs; Krishfield et al., 2008; Toole et al., 2011) deployed during 2015 (grey lines); an ITP deployed in 2007 (Jackson et al., 2012, blue line); and in the Eulerian and Lagrangian reference frame in the October 2015 marginal ice zone measurements (gold and purple points, respectively). For October 2015 measurements, closed circles represent initial HC values, open circles represent final HC values, and crosses represent oceanic heat flux based on the change between. Heat content is calculated for ITPs deployed in 2015 using  $h$  where  $\rho = 1,023 \text{ kg/m}^3$ . Ocean heat flux was parametrized from the ITP deployed in 2007 following the method of McPhee (1992). Negative values of ocean heat flux indicate that heat is transferred from the ocean to the atmosphere or sea ice.

Oceanic heat flux from seawater to ice is estimated as the product of heat and turbulence at the ice-ocean interface (Krishfield & Perovich, 2005). Direct measurements of this value are difficult to make, so it is often parametrized using a combination of mixed layer temperature and ice-ocean friction velocity (McPhee, 1992) or using sea ice thermistor profiles (McPhee & Untersteiner, 1982), both of which are possible using ice mass balance buoys. The former method was used by Jackson et al. (2012). We can alternatively estimate the oceanic heat flux with upper ocean temperature profiles as the change of upper ocean heat content over time ( $\Delta HC / \Delta t$ ), where it is assumed all heat loss is due to upward oceanic heat flux. Change in upper ocean heat content is calculated by integrating the temperature relative to freezing temperature (equation (1)).

We compare estimates of oceanic heat flux during the October 2015 marginal ice zone event with autumn ocean heat fluxes in 2007 (parametrized using ice-ocean friction velocity from an ITP and autonomous ocean flux buoy [AOFB, Jackson et al., 2012]) and in 2015 but in pack ice (estimated using temperature profiles from four ITPs (Toole et al., 2011) deployed in the Canada Basin between  $\sim 76$  and  $82^\circ\text{N}$ , i.e., north of the October marginal ice zone observation; Figure 7). The ITP used in Jackson et al. (2012) was deployed on an approximately 3 m thick ice floe, and the ITPs deployed in 2015 were on ice floes with thicknesses between 1.0 and 1.9 m. Ice thicknesses during the October marginal ice zone observations, by contrast, were on the order of 0.1 m. Oceanic heat flux for the October observations (gold and purple points, corresponding to Eulerian and Lagrangian as in Figure 1) and ITPs deployed in 2015 (grey lines) are determined as the rate of change of upper ocean heat contents. Corresponding initial and final upper ocean heat contents ( $HC$ ) are shown in the top of Figure 7 and are determined as described in equation (1) but with  $h$  defined for ITP profiles as the depth where  $\rho = 1,023 \text{ kg/m}^3$ , as that was empirically determined to be more consistently at or just below the MLD (see Appendix A). In addition, ITPs do not begin measuring data until about 6 m below the surface so the surface waters, including  $\rho = 1,022 \text{ kg/m}^3$ , are often not sampled. Heat content values based on the ITP profiles are significantly lower than those in Timmermans (2015), due to the shallower depth of integration used here, which generally excludes most of the warm NSTM.

The magnitude of heat content and flux during the October marginal ice zone observations are significantly larger than those observed in the autumn ITP time series. Upper ocean heat content observed throughout the marginal ice zone observations are larger than that observed by the ITP under thicker ice. Observations generally show negative ocean heat fluxes, indicating a loss of heat over time, with values around  $-100 \text{ W/m}^2$ . Heat flux values are more than twice as high as average flux observed by ITPs in the same period. Positive ocean heat flux values are occasionally observed by 2015 ITP profiles, and indicate an increase in heat content estimated for the upper ocean, possibly due to horizontal advection or other terms.

The thin, new ice at the advancing ice edge is likely to see much larger upper ocean heat entrainment events with strong negative heat fluxes in the autumn. Despite the significantly higher oceanic heat flux, a much smaller portion of the net heat flux is found to go into sea ice melt in thin ice than under thick ice. In Figure 6, between 60 and 70% of the ocean heat flux is directly lost to the atmosphere, with the remainder used to melt pancake ice. In comparison, Timmermans (2015) found nearly all of the heat loss was used for basal ice melt (of thicker pack ice), with less than 1/3 accounted for by conductive flux to the atmosphere.

Compared to basal melt of thick ice by oceanic heat entrainment, melt of thin sea ice may have more extreme consequences for future sea ice and snow cover. Loss of thin sea ice during autumn ice advance effectively resets the snow accumulation for the area in question. Webster et al. (2014) found that delayed freezeup in the Canada Basin is strongly correlated with thinner winter snow depth. As snow cover can both influence winter sea ice growth (Mellor, 1964) and maintain a higher surface albedo (Barry, 1996), the effect of this event may extend through the winter and into the following spring.

#### 4.2. Wave Effects

The October 2015 marginal ice zone event presented conditions that lie somewhere between the limiting cases of thick, multiyear ice and completely open water. One key difference between these limiting cases and the marginal ice zone is the presence of surface waves in ice, which are generally increasing in the western Arctic (e.g., Thomson et al., 2016). At lower latitudes, surface waves are known to enhance mixing of the upper ocean through the generation of Langmuir Turbulence and the shear in the Stokes drift profiles (D'Asaro et al., 2014). Globally, wave effects may produce mixed layers that are 20% deeper, on average (D'Asaro et al., 2014). Thus, the presence of waves in the October 2015 marginal ice zone event may have increased the amount of heat released from the upper ocean.

Here we explore how the conditions in this event compare to the limiting cases of thick ice studies (Jackson et al., 2012; Timmermans, 2015) and open water, the latter defined for wind speeds observed during the October 2015 event but without the presence of sea ice. We include results from the northern two SWIFT buoys (Figure 1), excluded from the analyses up this point, to further distinguish the wave conditions. The two northern buoys experienced smaller waves and an increase in ice rather than a decrease (Table 2). Figure 8 shows ranges of observed ice draft, wind speeds  $U_{10}$ , wave Stokes drift in the surface layer  $u_{s,SL}$ , and turbulent Langmuir number  $La^{-2}$ . Here surface layer Stokes drift is defined as the average Stokes drift from  $z = 0$  to  $z = 0.2 \text{ MLD}$ , as defined in D'Asaro et al. (2014). The Stokes drift is estimated from the observed wave spectra as

$$u_{s,SL}(z) = \frac{16\pi^3}{g} \int_0^\infty f^3 e^{-kz} E(f) df, \quad (6)$$

where  $f$  is frequency,  $E$  is energy density,  $k$  is wavenumber, and  $g$  is gravity. This is calculated for the open water case based on the fully developed wave spectra of Pierson and Moskowitz (1964) using observed wind speeds. For the ITP cases, we simply assume zero waves under thick ice. The Langmuir number,  $(La^{-2} = u_{s,SL}/U_{10})$ , is then used to compare relative strength of the wave forcing to the wind forcing (e.g., D'Asaro et al., 2014).

The wave forcing ( $u_{s,SL}$ ) decreases significantly across these cases, despite comparable wind forcing ( $U_{10}$ ). The Langmuir number is scaled by the wind, and thus has a similar signal. The signals are of course tied to the ice, because ice attenuates waves and limits the fetch available for wave generation. This suggests a feedback mechanism, in which ice formation can limit surface waves directly, indirectly limiting ocean heat fluxes. In contrast, wave growth may enhance mixing such that ocean heat fluxes are increased relative to pure wind forcing, and thus melting is promoted. Though not presented here, results show that these

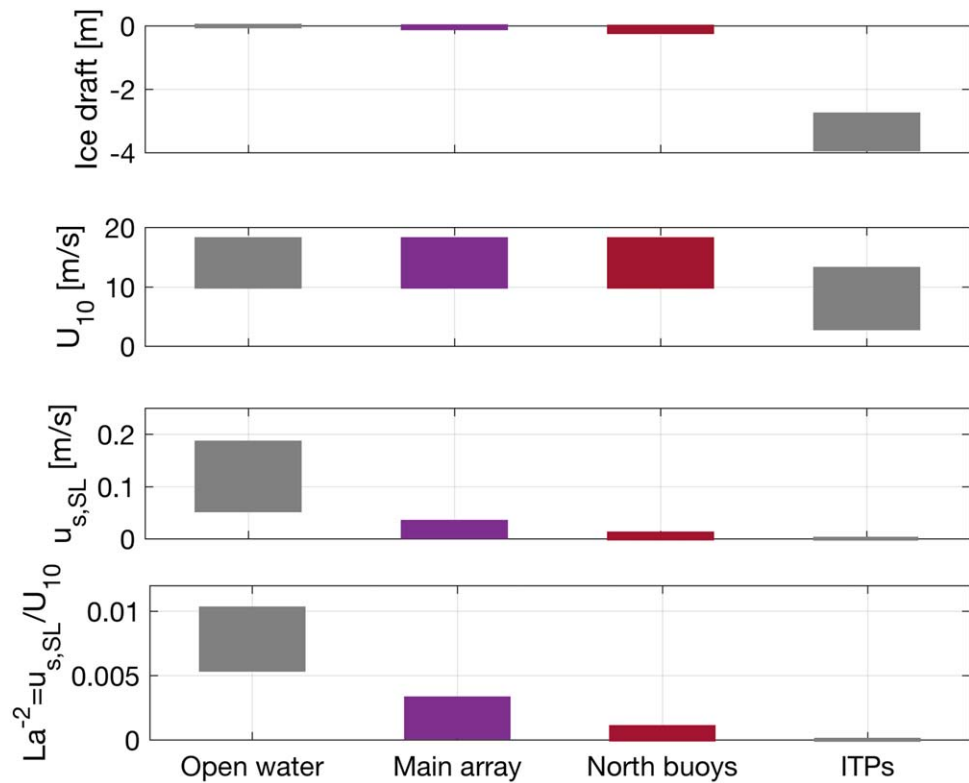


**Figure 8.** Comparison of ice, wind, and wave forcings observed in open water, during the 10–14 October event, and under thick ice observed by ITPs (Jackson et al., 2012; Timmermans, 2015). Observations during the 10–14 October 2015 event are separated out into the main array and northern SWIFT buoys, in purple and red, respectively.

feedbacks are dependent on the short (high-frequency) surface waves, which are most severely affected by ice and most important in setting the Stokes drift (i.e., the  $f^3$  dependence in equation (6)).

Here we will apply a nondimensional fetch scaling to interpret the observed wave forcing and provide guidance for future applications in ice-covered oceans. The two buoys to the north measured noticeably smaller waves (Table 2) as a result of the fetch-limited conditions in the open water embayment in which the buoys were deployed (Figure 1). Under fetch-limited conditions, wave height is a function of the fetch distance, such that nondimensional wave energy is directly related to nondimensional fetch (Young, 1999). Nondimensional fetch is defined as

$$\chi = \frac{gx}{U^2}, \quad (7)$$

where  $g$  is gravitational acceleration,  $x$  is the dimensional fetch distance, and  $U$  is wind speed. Approximate dimensional fetch distances to ice or land are calculated as described in Thomson and Rogers (2014). Nondimensional wave energy ( $E$ ) is defined as

$$E = \frac{g^2 H_s^2}{16U^4}, \quad (8)$$

where  $H_s$  is the significant wave height. Under a constant wind forcing, wave energy (height) will increase exponentially with increasing fetch.

In fact, the waves in this marginal ice zone event do scale by fetch. Figure 9 compares the nondimensional fetch and nondimensional energy of waves in the main array and the north pair. Along the main array, wave energy scales with fetch by the relationship  $E \sim \chi^{1.6}$  (purple points). The wave energy of the northern SWIFT buoys scales with fetch according to  $E \sim \chi^{0.88}$  (red points). Both relationships fall within the range of exponential values described by conventional open water fetch relationships (Young, 1999), which have previously been shown to hold in the Arctic Ocean (Smith & Thomson, 2016; Thomson & Rogers, 2014).

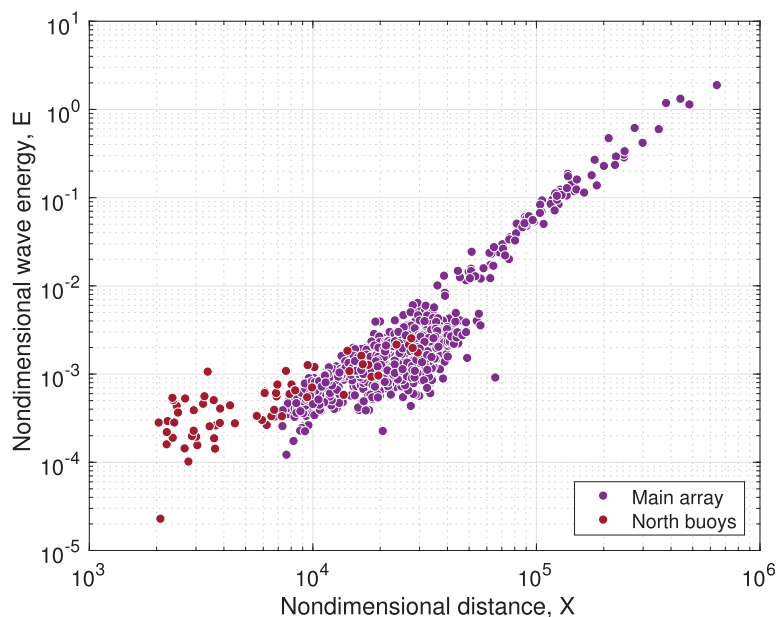


**Figure 9.** Comparison of nondimensional fetch and nondimensional energy from SWIFT buoys in main array (purple) and northern SWIFT buoys (red).

However, we see that wave energy at the northern buoys is limited not just by the decreasing fetch distances as the embayment closes up but also by the presence of ice which limits the “effective fetch” distance over which waves can grow in partially ice-covered ocean (Smith & Thomson, 2016). The exponential relationship between fetch and energy then has a lower power as a result of partial ice cover at the location of the northern SWIFT buoys. In contrast, as ice along the main array melts and SWIFT buoys drift north, the fetch becomes larger and wave heights continue to grow. As a result, the range of Langmuir numbers is much higher for the main array than for the northern SWIFT buoys (Figure 8). This suggests that in the future, specific details of air-ice-ocean interactions and release of upper ocean heat may be sensitive to effective fetch.

We speculate that the variation in the wave forcing accounts for the variation in the outcome of this event. While initial upper ocean heat content and wind speeds were similar between the northern SWIFTs and the main array, there are strong differences in the evolution of surface waves, and opposing trends in sea ice (Table 2). For the northern buoys, ice formation was sufficient to limit the wave growth and associated processes. For the main array, the release of ocean heat was substantial, and ice melt was sufficient to maintain wave growth. The spatial differences may also be a result of ocean preconditioning, such as associated with nonlinear ice retreat (e.g., Steele & Ermold, 2015), but the observations actually show more initial heat content in the ocean under the north buoys rather than less. Without observations of the final ocean heat values for the northern SWIFTs, we are unable to determine conclusively whether surface wave forcing, ocean preconditioning, or other factors led to the different fates of sea ice at these two locations.

With the expansion of seasonally ice-free area in the western Arctic, increasingly large areas are undergoing autumn freezeup (Galley et al., 2016). As thin ice and large open water fetches become more common (Kwok & Rothrock, 2009; Thomson & Rogers, 2014), the role of upper ocean heat on delaying ice advance may be greater. It is important for models to be able to capture episodic storm events such as the October 2015 marginal ice zone observations described here. Such events clearly have a rapid impact on sea ice at the operational forecast level. They are additionally important for better estimating the fate of stored upper ocean heat under the winter ice cover, which is a critical parameter in models at the climate and inter-annual level. However, most current operational and research models are not yet up to the task (Gent et al., 2011; Metzger et al., 2014). In order to fully capture this event, a model would need to predict sufficient wind and waves, entrainment of upper ocean heat, and the rate of heat flux to the sea ice and atmosphere. Though this coupling is beyond current model capabilities, this highlights the importance of high-

resolution, fully coupled models for the Arctic. Continuing to advance our understanding of the many ways in which ocean heat contributes to thinning and retreat of Arctic sea ice is essential for future projections (Carmack et al., 2015).

## 5. Conclusions

Observations of an autumn storm in the Beaufort Sea illustrate how an event can temporarily reverse the seasonal ice edge advance. Prior to the in situ observations, pancake ice was formed by surface waves and strong negative atmospheric heat fluxes. As the event progressed, ocean heat was released, and most of the newly formed ice melted. The event was remarkable, relative to climatology, in the magnitude and extent of the ocean heat flux. Furthermore, pancake ice and large surface waves have been only rarely observed in the Canada Basin.

The key observations and results are summarized as follows:

1. An autumn high-wind event in the Beaufort Sea released a large amount of stored solar heat from the ocean mixed layer and near-surface temperature maximum (NSTM).
2. A significant portion of heat released was used to melt thin, new pancake ice that had recently formed as part of the seasonal ice advance.
3. The rate of ocean heat release is larger than that observed in prior studies under thick Arctic ice, with a much larger fraction accounted for by convective flux to the atmosphere.
4. The magnitude of heat released and sea ice melted may be related to the changing wave climate in the Arctic Ocean.

Although entrainment of upper ocean heat has been observed under multiyear ice in the Canada Basin, the observations presented here indicate that this mechanism can also melt new sea ice and, in fact, control the rate of ice advance in the marginal ice zone, an area that is increasing as the Arctic Ocean transitions to a seasonal sea ice cover (Meier et al., 2014). Under multiyear ice, rapid ocean heat flux and ice melt occurs primarily in the summer and early autumn, when solar heat inputs are largest. The magnitude of this event is much larger than events observed in autumn under multiyear ice, and indicates that stored solar heat can have an impact over much more of the year with thinner ice cover.

The magnitude of this event may have been enhanced by the strong wave climate as well as the high winds, both of which are expected to be generally increasing. The average winds associated with Arctic cyclones have been increasing over the last few decades, and so stronger winds may occur more frequently in the future (Asplin et al., 2015; Serreze et al., 2001). Wave events of this magnitude are rare in the Arctic basin, and only occur at most a few times within a given autumn. However, this probability appears to be increasing (Thomson et al., 2016). Attenuation of high-frequency waves is a plausible feedback to suppress wave-driven mixing during ice edge advance. Either way, the increasing surface wave climate in the western Arctic is having at least one noticeable affect: the prevalence of pancake ice during ice advance.

Following the storm, the ice re-formed, and the ice edge advanced over this area just a few days later. A few days of reversal in ice edge advance may not seem consequential to the overall seasonal cycle. However, the net thermodynamic ice growth through the autumn and winter may be significantly less as a result of events such as this one. Additionally, delayed autumn freezeup in the Beaufort region has been found to be strongly correlated with thinner snow cover on sea ice (Webster et al., 2014), which results in a lower surface albedo (Perovich & Polashenski, 2012).

## Appendix A: Budget Depths

Using heat and salt budgets (equations (3) and (4)) to understand evolution of the upper ocean requires appropriate choice of depth over which they should be integrated. Though there are a variety of choices of  $h$  that seem reasonable to use as the definition of the bottom of the “upper ocean” based on temperature profiles and prior literature, the correct choice of  $h$  is not immediately obvious. Here we will explore a number of possible choices of  $h$  and their impacts, ordered by increasing depth:

1. MLD. This is the method used in Jackson et al. (2012).



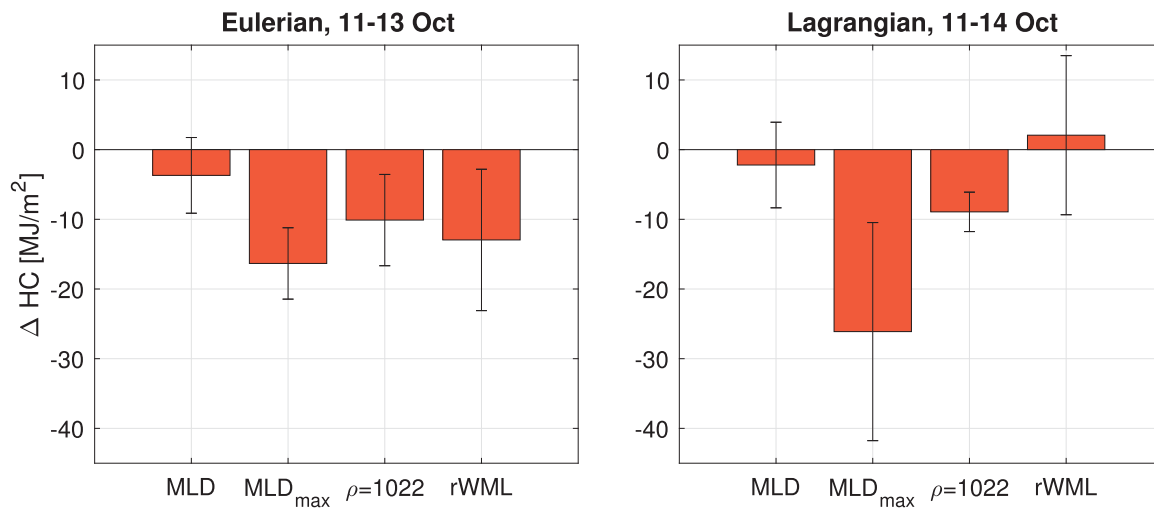


**Figure A1.** Comparison of change in heat content ( $\Delta HC$ ; equation (1)) calculated using four different methods of defining  $h$ . Values are compared for the Eulerian reference frame on the left, and Lagrangian reference frame on the right. Error bars are the standard deviation from each set of estimates.

2. Maximum MLD over the time series of each station or buoy ( $MLD_{max}$ ) such that a single depth results in a constant volume of integration.
3. A constant density isopycnal that is unaffected by mixing; i.e., always below MLD. Here the  $\rho = 1,022 \text{ kg/m}^3$  isopycnal is chosen as it is observed to be below final MLDs.
4. Temperature minimum of the rWML (approximately 40–50 m). This is the method used in Timmermans (2015).

We will use the resulting change in heat content  $\Delta HC$ , the left-hand side term in the heat budget (equation (3)), to understand the implications of each choice of  $h$  (Figure A1). The results presented in the main body of the paper use the third method. The methods are detailed and compared below.

1. Jackson et al. (2012) observed the change in heat content from the surface to the base of the surface mixed layer (MLD) to track diffusion of heat into the mixed layer. This will estimate heat that is lost from the mixed layer into the ice or atmosphere. However, in this study, the observed atmospheric heat flux is greater than the heat content calculated using this method (Figure 6), suggesting additional heat lost from below the MLD (Figures 2 and 3). Using the MLD as the bottom depth of integration will not capture any heat from the NSTM, which appears to comprise a substantial amount of heat lost from the upper ocean. In fact, the estimates of changes in heat content made using this definition of  $h$  are smaller than any others, and even show an increase in heat at some locations as indicated by the error bars.
2. Although it is initially tempting to use a constant depth of integration, such as the maximum MLD over each record, we can see the danger of this choice by examining salinity profiles in the Lagrangian reference frame in Figure 4. Over these deployments, there is substantial vertical advection due to inertial pumping of the MLD and isopycnal below. As a result, the change in heat content is drastically overestimated in the Lagrangian reference frame (nearly twice that estimated in the Eulerian reference frame).
3. Using an  $h$  that follows an isopycnal accounts for changes due to vertical advection, and thus avoids the problem in the preceding method. We define  $h$  with a constant isopycnal that lies below the depths affected by mixing (i.e., the MLD). Defining a depth that is just below the MLD will allow all heat content changes due to mixing to be included. We observe that the  $1,022 \text{ kg/m}^3$  isopycnal lies below the MLD (thick line) the majority of the time and is approximately the depth of the MLD at the final time (Figures 2 and 3). The change in heat content using this  $h$  is consistent between the two reference frames, and consistent with what we qualitatively observe in the temperature profiles (Figure 4).
4. Timmermans (2015) use the rWML depth, which is well below the MLD and NSTM, to examine changes in stored solar heat over the annual cycle. In Figures 2 and 3, we can see this temperature minimum is generally around 40–50 during this event. This depth allows the heat budget to include all water masses containing summer solar heat, and is well below the depth that may be effected by entrainment events.

However, this choice is problematic for this event in that the near-surface temperature maximum is seen to be quite spatially variable (Figure 2), and the Lagrangian buoys will drift with the mixed layer into areas where the NSTM has less initial heat. As a result, this method will result in reasonable estimates of change in heat content for the Eulerian reference frame, but will significantly underestimate change in heat content in the Lagrangian reference frame due to different initial NSTM heat content further north.

In summary, we determine the 1,022 kg/m<sup>3</sup> isopycnal to best capture the upper ocean evolution that occurs during this event. Though there are likely other appropriate definitions of  $h$  that could be used to describe the upper ocean here, we find that this definition adequately suites our purposes. Whenever  $h$  is used throughout the paper, it is defined as the depth at which  $\rho = 1,022 \text{ kg/m}^3$ .

## Acknowledgments

This work was supported by the Office of Naval Research as part of the “Sea State and Boundary Layer Physics of the Emerging Arctic Ocean” Departmental Research Initiative, initiated by Scott Harper and Martin Jeffries. The funding was award N00014-13-1-0284. The Sea State data used are available from the Sea State laboratory under the Data tab at [www.apl.uw.edu/arcticseastate](http://www.apl.uw.edu/arcticseastate). The Ice-Tethered Profiler data were collected and made available by the Ice-Tethered Profiler Program (Krishfield et al., 2008; Toole et al., 2011) based at the Woods Hole Oceanographic Institution (<http://www.whoi.edu/itp>). We thank Alex de Klerk, Joe Talbert, and the crew of the *R/V Sikuliaq* for their assistance in data collection, and Eric D’Asaro for valuable feedback on an early version of this manuscript. Thanks to two anonymous reviewers whose comments greatly improved the manuscript.

## References

- Asplin, M. G., Fissel, D. B., Papakyriakou, T. N., & Barber, D. G. (2015). Synoptic climatology of the Southern Beaufort Sea troposphere with comparisons to surface winds. *Atmosphere-Ocean*, 53(2), 264–281. <https://doi.org/10.1080/07055900.2015.1013438>
- Asplin, M. G., Galley, R., Barber, D. G., & Prinsenberg, S. (2012). Fracture of summer perennial sea ice by ocean swell as a result of Arctic storms. *Journal of Geophysical Research*, 117, C06025. <https://doi.org/10.1029/2011JC007221>
- Asplin, M. G., Scharien, R., Else, B., Howell, S., Barber, D. G., Papakyriakou, T., et al. (2014). Implications of fractured Arctic perennial ice cover on thermodynamic and dynamic sea ice processes. *Journal of Geophysical Research: Oceans*, 119, 2327–2343. <https://doi.org/10.1002/2013JC009557>
- Barry, R. G. (1996). The parameterization of surface albedo for sea ice and its snow cover. *Progress in Physical Geography*, 20(1), 63–79.
- Barthélemy, A., Fichefet, T., Goosse, H., & Madec, G. (2015). Modeling the interplay between sea ice formation and the oceanic mixed layer: Limitations of simple brine rejection parameterizations. *Ocean Modelling*, 86, 141–152. <https://doi.org/10.1016/j.ocemod.2014.12.009>
- Carmack, E. I., Polyakov, L., Padman, L., Fer, E., Hunke, J., Hutchings, J., et al. (2015). Toward quantifying the increasing role of oceanic heat in sea ice loss in the new Arctic. *Bulletin of the American Meteorological Society*, 96(12), 2079–2105. <https://doi.org/10.1175/BAMS-D-13-00177.1>
- Collins, C., Blomquist, B., Persson, O., Lund, B., Rogers, W., Thomson, J., et al. (2017). Doppler correction of wave frequency spectra measured by underway vessels. *Journal of Atmospheric and Oceanic Technology*, 34(2), 429–436. <https://doi.org/10.1175/JTECH-D-16-0138.1>
- Collins, C. O., Rogers, W. E., Marchenko, A., & Babanin, A. V. (2015). In situ measurements of an energetic wave event in the Arctic marginal ice zone. *Geophysical Research Letters*, 42, 1863–1870. <https://doi.org/10.1002/2015GL063063>
- Cronin, M. F., Bond, N. A., Farrar, J. T., Ichikawa, H., Jayne, S. R., Kawai, Y., et al. (2013). Formation and erosion of the seasonal thermocline in the Kuroshio extension recirculation gyre. *Deep Sea Research Part II: Topical Studies in Oceanography*, 85, 62–74. <https://doi.org/10.1016/j.dsr2.2012.07.018>
- Cronin, M. F., Pelland, N. A., Emerson, S. R., & Crawford, W. R. (2015). Estimating diffusivity from the mixed layer heat and salt balances in the North Pacific. *Journal of Geophysical Research: Oceans*, 120, 7346–7362. <https://doi.org/10.1002/2015JC011010>
- D’Asaro, E. A., Thomson, J., Shcherbina, A. Y., Harcourt, R. R., Cronin, M. F., Hemer, M. A., et al. (2014). Quantifying upper ocean turbulence driven by surface waves. *Geophysical Research Letters*, 41, 1–6. <https://doi.org/10.1002/2013GL058193>
- Eicken, H., Lensu, M., Leppäranta, M., Tucker, W., Gow, A., & Salmela, O. (1995). Thickness, structure, and properties of level summer multi-year ice in the Eurasian sector of the Arctic Ocean. *Journal of Geophysical Research*, 100(C11), 22697–22710. <https://doi.org/10.1029/95JC02188>
- Forristall, G. Z. (1981). Measurements of a saturated range in ocean wave spectra. *Journal of Geophysical Research*, 86(C9), 8075–8084. <https://doi.org/10.1029/JC086iC09p08075>
- Galley, R., Babb, D., Ogi, M., Else, B., Geilfus, N.-X., Crabeck, O., et al. (2016). Replacement of multiyear sea ice and changes in the open water season duration in the Beaufort Sea since 2004. *Journal of Geophysical Research: Oceans*, 121, 1806–1823. <https://doi.org/10.1002/2015JC011583>
- Gent, P. R., G., Danabasoglu, L. J., Donner, M. M., Holland, E. C., Hunke, S. R., Jayne, D. M., et al. (2011). The community climate system model version 4. *Journal of Climate*, 24(19), 4973–4991. <https://doi.org/10.1175/2011JCLI4083.1>
- Guest, P., Persson, P. O., Wang, G., Jordan, S., Yin, M., Blomquist, Y., et al. (2018). Low-level baroclinic jets over the new Arctic Ocean. *Journal of Geophysical Research: Oceans*, 123. <https://doi.org/10.1002/2018JC013778>
- Herbers, T. H. C., Jessen, P. F., Janssen, T. T., Colbert, D. B., & MacMahan, J. H. (2012). Observing ocean surface waves with GPS-tracked buoys. *Journal of Atmospheric and Oceanic Technology*, 29, 944–959. <https://doi.org/10.1175/JTECH-D-11-00128.1>
- Ivanov, V., Alexeev, V., Koldunov, N. V., Repina, I., Sando, A. B., Smedsrud, L. H., et al. (2016). Arctic Ocean heat impact on regional ice decay: A suggested positive feedback. *Journal of Physical Oceanography*, 46(5), 1437–1456. <https://doi.org/10.1175/JPO-D-15-0144.1>
- Jackson, J. M., Allen, S. E., McLaughlin, F., Woodgate, R., & Carmack, E. (2011). Changes to the near-surface waters in the Canada Basin, Arctic Ocean from 1993–2009: A basin in transition. *Journal of Geophysical Research*, 116, C10008. <https://doi.org/10.1029/2011JC007069>
- Jackson, J. M., Williams, W. J., & Carmack, E. C. (2012). Winter sea-ice melt in the Canada Basin, Arctic Ocean. *Geophysical Research Letters*, 39, L03603. <https://doi.org/10.1029/2011GL050219>
- Jackson, M., Carmack, E. C., McLaughlin, F. A., Allen, S. E., & Ingram, R. G. (2010). Identification, characterization, and change of the near-surface temperature maximum in the Canada Basin, 1993–2008. *Journal of Geophysical Research*, 115, C05021. <https://doi.org/10.1029/2009JC005265>
- Jeffries, M. O., Overland, J. E., & Perovich, D. K. (2013). The Arctic shifts to a new normal. *Physics Today*, 66(10), 35–40.
- Khandekar, M. (1980). Inertial oscillations in floe motion over the Beaufort Sea—Observations and analysis. *Atmosphere-Ocean*, 18(1), 1–14. <https://doi.org/10.1080/07055900.1980.9649073>
- Krishfield, R., Toole, J., Proshutinsky, A., & Timmermans, M.-L. (2008). Automated ice-tethered profilers for seawater observations under pack ice in all seasons. *Journal of Atmospheric and Oceanic Technology*, 25(11), 2091–2105. <https://doi.org/10.1175/2008JTECH0587.1>
- Krishfield, R. A., & Perovich, D. K. (2005). Spatial and temporal variability of oceanic heat flux to the Arctic ice pack. *Journal of Geophysical Research*, 110, C07021. <https://doi.org/10.1029/2004JC002293>
- Kwok, R., & Rothrock, D. (2009). Decline in Arctic sea ice thickness from submarine and ICESat records: 1958–2008. *Geophysical Research Letters*, 36, L15501. <https://doi.org/10.1029/2009GL039035>

- Loose, B., McGillis, W., Schlosser, P., Perovich, D., & Takahashi, T. (2009). Effects of freezing, growth, and ice cover on gas transport processes in laboratory seawater experiments. *Geophysical Research Letters*, 36, L05603. <https://doi.org/10.1029/2008GL036318>
- Lund, B., Graber, H., Smith, C., Doble, M., Persson, M., Thomson, O. J., et al. (2018). Arctic sea ice drift measured by shipboard marine radar. *Journal of Geophysical Research: Oceans*, 123. <https://doi.org/10.1029/2018JC013769>
- Lygre, A., & Krogstad, H. E. (1986). Maximum entropy estimation of the directional distribution in ocean wave spectra. *Journal of Physical Oceanography*, 16(12), 2052–2060. [https://doi.org/10.1175/1520-0485\(1986\)016<2052:MEEOTD>2.0.CO;2](https://doi.org/10.1175/1520-0485(1986)016<2052:MEEOTD>2.0.CO;2)
- Maykut, G., & McPhee, M. G. (1995). Solar heating of the Arctic mixed layer. *Journal of Geophysical Research*, 100(C12), 24691–24703. <https://doi.org/10.1029/95JC02554>
- Maykut, G. A. (1978). Energy exchange over young sea ice in the central Arctic. *Journal of Geophysical Research*, 83(C7), 3646–3658. <https://doi.org/10.1029/JC083iC07p03646>
- McLaughlin, F., Carmack, E., Proshutinsky, A., Krishfield, R. A., Guay, C., Yamamoto-Kawai, M., et al. (2011). The rapid response of the Canada Basin to climate forcing: From bellwether to alarm bells. *Oceanography*, 24(3), 146–159. Retrieved from <http://www.jstor.org/stable/24861309>
- McPhee, M. G. (1992). Turbulent heat flux in the upper ocean under sea ice. *Journal of Geophysical Research*, 97(C4), 5365–5379. <https://doi.org/10.1029/92JC00239>
- McPhee, M. G., & Untersteiner, N. (1982). Using sea ice to measure vertical heat flux in the ocean. *Journal of Geophysical Research*, 87(C3), 2071–2074. <https://doi.org/10.1029/JC087iC03p02071>
- Meier, W. N. (2017). Losing Arctic sea ice: Observations of the recent decline and the long-term context. In *Sea ice* (pp. 290–303). Chichester, UK: John Wiley.
- Meier, W. N., Hovelsrud, G. K., Oort, B. E., Key, J. R., Kovacs, K. M., Michel, C., et al. (2014). Arctic sea ice in transformation: A review of recent observed changes and impacts on biology and human activity. *Reviews of Geophysics*, 52, 185–217. <https://doi.org/10.1002/2013RG000431>
- Mellor, M. (1964). *Properties of snow*. Hanover, NH: United States Army Corps of Engineers, Cold Regions Research and Engineering Laboratory.
- Metzger, E. J., Smedstad, O. M., Thoppil, P. G., Hurlburt, H. E., Cummings, J. A., Wallcraft, A. J., et al. (2014). US Navy operational global ocean and Arctic ice prediction systems. *Oceanography*, 27(3), 32–43. Retrieved from <http://www.jstor.org/stable/24862187>
- Ono, N. (1966). Thermal properties of sea ice. III. On the specific heat of sea ice. *Low Temperature Science A*, 24, 249–258.
- Peralta-Ferriz, C., & Woodgate, R. A. (2015). Seasonal and interannual variability of pan-Arctic surface mixed layer properties from 1979 to 2012 from hydrographic data, and the dominance of stratification for multiyear mixed layer depth shoaling. *Progress in Oceanography*, 134, 19–53. <https://doi.org/10.1016/j.pocean.2014.12.005>
- Perovich, D. K., Light, B., Eicken, H., Jones, K. F., Runciman, K., & Nghiem, S. V. (2007). Increasing solar heating of the Arctic Ocean and adjacent seas, 1979–2005: Attribution and role in the ice-albedo feedback. *Geophysical Research Letters*, 34, L19505. <https://doi.org/10.1029/2007GL031480>
- Perovich, D. K., & Polashenski, C. (2012). Albedo evolution of seasonal Arctic sea ice. *Geophysical Research Letters*, 39, L08501. <https://doi.org/10.1029/2012GL051432>
- Perovich, D. K., Richter-Menge, J. A., Jones, K. F., & Light, B. (2008). Sunlight, water, and ice: Extreme Arctic sea ice melt during the summer of 2007. *Geophysical Research Letters*, 35, L11501. <https://doi.org/10.1029/2008GL034007>
- Persson, P. O. G. (2012). Onset and end of the summer melt season over sea ice: Thermal structure and surface energy perspective from sheba. *Climate Dynamics*, 39, 1349–1371. <https://doi.org/10.1007/s00382-011-1196-9>
- Pierson, W. J., & Moskowitz, L. (1964). A proposed spectral form for fully developed wind seas based on the similarity theory of S. A. Kitai-gorodskii. *Journal of Geophysical Research*, 69(24), 5181–5190. <https://doi.org/10.1029/JZ069i024p05181>
- Polyakov, I. V., Pnyushkov, A. V., Rember, R., Padman, L., Carmack, E. C., & Jackson, J. M. (2013). Winter convection transports Atlantic water heat to the surface layer in the eastern Arctic Ocean. *Journal of Physical Oceanography*, 43(10), 2142–2155. <https://doi.org/10.1175/JPO-D-12-0169.1>
- Roach, A., Aagaard, K., & Carsey, F. (1993). Coupled ice-ocean variability in the Greenland Sea. *Atmosphere-Ocean*, 31(3), 319–337. <https://doi.org/10.1080/07055900.1993.9649474>
- Rogers, W. E., Thomson, J., Shen, H. H., Doble, M. J., Wadhams, P., & Cheng, S. (2016). Dissipation of wind waves by pancake and frazil ice in the autumn Beaufort Sea. *Journal of Geophysical Research: Oceans*, 121, 7991–8007. <https://doi.org/10.1002/2016JC012251>
- Sellers, W. D. (1974). Heat transfer in soil. In *Physical climatology* (5th ed.). Chicago, IL: University of Chicago Press.
- Serreze, M. C., Lynch, A. H., & Clark, M. P. (2001). The arctic frontal zone as seen in the NCEP–NCAR reanalysis. *Journal of Climate*, 14(7), 1550–1567. [https://doi.org/10.1175/1520-0442\(2001\)014<1550:TAFZAS>2.0.CO;2](https://doi.org/10.1175/1520-0442(2001)014<1550:TAFZAS>2.0.CO;2)
- Simmonds, I., & Keay, K. (2009). Extraordinary September Arctic sea ice reductions and their relationships with storm behavior over 1979–2008. *Geophysical Research Letters*, 36, L19715. <https://doi.org/10.1029/2009GL039810>
- Smith, M., & Thomson, J. (2016). Scaling observations of surface waves in the Beaufort Sea. *Elementa Science of the Anthropocene*, 4, 97. <https://doi.org/10.12952/journal.elementa.000097>
- Spren, G., Kaleschke, L., & Heygster, G. (2008). Sea ice remote sensing using AMSR-E 89-GHz channels. *Journal of Geophysical Research: Oceans*, 113, C02S03. <https://doi.org/10.1029/2005JC003384>
- Stammerjohn, S., Massom, R., Rind, D., & Martinson, D. (2012). Regions of rapid sea ice change: An inter-hemispheric seasonal comparison. *Geophysical Research Letters*, 39, L06501. <https://doi.org/10.1029/2012GL050874>
- Steele, M., & Ermold, W. (2015). Loitering of the retreating sea ice edge in the Arctic seas. *Journal of Geophysical Research: Oceans*, 120, 7699–7721. <https://doi.org/10.1002/2015JC011182>
- Steele, M., Ermold, W., & Zhang, J. (2011). Modeling the formation and fate of the near-surface temperature maximum in the Canadian Basin of the Arctic Ocean. *Journal of Geophysical Research*, 116, C11015. <https://doi.org/10.1029/2010JC006803>
- Stopa, J. E. (2016). Wave climate in the Arctic 1992–2014: Seasonality and trends. *The Cryosphere*, 10(4), 1605. <https://doi.org/10.5194/tc-10-1605-2016>
- Stroeve, J., Markus, T., Boisvert, L., Miller, J., & Barrett, A. (2014). Changes in Arctic melt season and implications for sea ice loss. *Geophysical Research Letters*, 41, 1216–1225. <https://doi.org/10.1002/2013GL058951>
- Stroeve, J. C., Crawford, A. D., & Stammerjohn, S. (2016). Using timing of ice retreat to predict timing of fall freeze-up in the Arctic. *Geophysical Research Letters*, 43, 6332–6340. <https://doi.org/10.1002/2016GL069314>
- Thomson, J. (2012). Wave breaking dissipation observed with SWIFT drifters. *Journal of Atmospheric and Oceanic Technology*, 29, 1866–1882. <https://doi.org/10.1175/JTECH-D-12-00018.1>
- Thomson, J. (2015). *ONR sea state DRI cruise report* (Rep. SKQ2015125). R/V Sikuliaq, Fall 2015.

- Thomson, J., Fan, Y., Stammerjohn, S., Stopa, J., Rogers, W. E., Girard-Ardhuin, F., et al. (2016). Emerging trends in the sea state of the Beaufort and Chukchi Seas. *Ocean Modelling*, 105, 1–12. <https://doi.org/10.1016/j.ocemod.2016.02.009>
- Thomson, J., & Rogers, W. E. (2014). Swell and sea in the emerging Arctic Ocean. *Geophysical Research Letters*, 14, 3136–3140. <https://doi.org/10.1002/2014GL059983>
- Thomson, J., Ackley, S., Girard-Ardhuin, S., Ardhuin, F., Babanin, F., Bidlot, A., et al. (2018). Overview of the Arctic sea state and boundary layer physics program. *Journal of Geophysical Research: Oceans*, 123. <https://doi.org/10.1002/2018JC013766>
- Timmermans, M.-L. (2015). The impact of stored solar heat on Arctic sea ice growth. *Geophysical Research Letters*, 42, 6399–6406. <https://doi.org/10.1002/2015GL064541>
- Toole, J. M., Krishfield, R. A., Timmermans, M.-L., & Proshutinsky, A. (2011). The ice-tethered profiler: Argo of the Arctic. *Oceanography*, 24(3), 126–135. Retrieved from <http://www.jstor.org/stable/24861307>
- Ullman, D. S., & Hebert, D. (2014). Processing of underway CTD data. *Journal of Atmospheric and Oceanic Technology*, 31(4), 984–998. <https://doi.org/10.1175/JTECH-D-13-00200.1>
- Wadhams, P., Aulicino, G., Parmiggiani, F., Persson, P., & Holt, B. (2018). Pancake ice thickness mapping in the Beaufort Sea from wave dispersion observed in SAR imagery. *Journal of Geophysical Research: Oceans*. <https://doi.org/10.1002/2017JC013003>
- Webster, M. A., Rigor, I. G., Nghiem, S. V., Kurtz, N. T., Farrell, S. L., Perovich, D. K., et al. (2014). Interdecadal changes in snow depth on Arctic sea ice. *Journal of Geophysical Research: Oceans*, 119, 5395–5406. <https://doi.org/10.1002/2014JC009985>
- Weeks, W. F., & Ackley, S. F. (1986). The growth, structure, and properties of sea ice. In *The geophysics of sea ice* (pp. 9–164). Berlin, Germany: Springer.
- Worby, A. P. (1999). *Observing Antarctic sea ice: A practical guide for conducting sea ice observations from vessels operating in the Antarctic pack ice*. A CD-ROM produced for the Antarctic Sea Ice processes and Climate (ASPeCt) program of the Scientific Committee for Antarctic Research (SCAR) Global Change (GLOCHANT) program, Hobart, Tas, Australia.
- Worby, A. P., Geiger, C. A., Paget, M. J., Van Woert, M. L., Ackley, S. F., & DeLiberty, T. L. (2008). Thickness distribution of Antarctic sea ice. *Journal of Geophysical Research*, 113, C05S92. <https://doi.org/10.1029/2007JC004254>
- Yang, J., Comiso, J., Walsh, D., Krishfield, R., & Honjo, S. (2004). Storm-driven mixing and potential impact on the Arctic Ocean. *Journal of Geophysical Research*, 109, C04008. <https://doi.org/10.1029/2001JC001248>
- Young, I. (1999). *Wind generated ocean waves, ocean engineering* (Vol. 2). Amsterdam, the Netherlands: Elsevier.
- Zippel, S., & Thomson, J. (2016). Air-sea interactions in the marginal ice zone. *Elementa Science of the Anthropocene*, 4, 95. <https://doi.org/10.12952/journal.elementa.000095>